A. Martinelli, C. Buonagura, C. Giordano, F. Topputo
Stochastic Optimization Through Nonlinear Covariance Mapping: Application to Weak Stability Boundary Transfers
Journal of Guidance Control and Dynamics, published online 10/04/2026
doi:10.2514/1.G009049

Stochastic Optimization through Nonlinear Uncertainty Mapping: Application to Weak Stability Boundary Transfers

Alessandro Martinelli*, Carmine Buonagura†, Carmine Giordano‡, and Francesco Topputo§
Politecnico di Milano, 20156 Milan, Italy

The advent of CubeSats for space exploration has underscored the need for a more stochastic-oriented mission analysis. Due to their limited orbital control authority and significant command execution errors, CubeSat missions are more vulnerable to space flight uncertainty. As a result, mission analysts are increasingly seeking optimal solutions from a stochastic perspective, by embedding uncertainties into the optimization phase. In this work, uncertainties related to initial conditions, maneuvers execution, and navigation are incorporated into a stochastic trajectory optimization process. The proposed method leverages a novel implementation of the unscented transformation, where a continuous propagation map avoids the simplification associated with sigma points resampling. With this approach, the problem is formulated as a nonlinear programming problem. In addition, an optimal guidance strategy is developed and compared to traditional strategies. The method is applied to weak stability boundary transfers, using the LUMIO CubeSat mission as the case study. This marks a novel and significant application. Results show that stochastic optimization can generate new nominal trajectories that require less fuel and are more robust, if compared to those obtained through deterministic optimization only.

I. Introduction

Mission analysis deals with space flight trajectory optimization by minimizing an objective function, such as the control effort or the time of flight, while satisfying a set of constraints. This optimization yields a nominal trajectory to follow and the control commands to be executed throughout the space flight. However, real-life uncertainties make it impossible to adhere to the nominal path. Uncertainties stem mainly from three sources of errors: actuation, navigation, and dynamical modeling [1]. Actuation errors represent the difference between the desired thrust action and its real execution. As such, they affect the control of the spacecraft. Navigation errors represent, instead, the difference between the real trajectory and its estimate. They affect the knowledge of the spacecraft trajectory. Errors in the dynamical model are due to its difference with the real dynamics. They arise from model simplifications, unknown

*Ph.D. Student, Department of Aerospace Science and Technology, alessandro2.martinelli@polimi.it.
†Ph.D. Student, Department of Aerospace Science and Technology, carmine.buonagura@polimi.it.
‡PostDoc Fellow, Department of Aerospace Science and Technology, carmine.giordano@polimi.it, AIAA Member.
§Full Professor, Department of Aerospace Science and Technology, francesco.topputo@polimi.it, AIAA Senior Member.

forces acting on the spacecraft, and the imperfect knowledge of the model parameters. Additionally, mission analysis often deals with uncertain initial conditions. These are the results of the uncertainties of the launcher trajectory, which produce errors in the orbital injection of the spacecraft.

In practice, mission analysis deals with uncertainties in a sequential approach [2]: first, a nominal trajectory is produced as the result of a deterministic optimization process; afterward, the effect of the uncertainties is considered with a navigation assessment. During the latter, both knowledge and dispersion analysis are carried out. Here, knowledge and dispersion represent the stochastic distance of the real trajectory from the estimated and nominal ones, respectively. Based on these two analyses, the navigation cost can be evaluated. The total cost of the mission, i.e., the ΔV, is given by the sum of the deterministic cost of the nominal trajectory and the stochastic navigation cost. By definition, the sequential approach is sub-optimal, as only the deterministic cost is optimized, while the stochastic one is simply evaluated. This approach is appropriate for traditional space missions, characterized by generous propellant budgets and a navigation cost constituting a minute fraction of the deterministic cost. The advent of miniaturized platforms for space exploration, such as the interplanetary CubeSats [3], calls for a paradigm shift in space mission analysis. These systems have skeletal propellant budgets, and are prone to large actuation and navigation uncertainties, mainly due to immature technologies. These uncertainties expand further when CubeSats fly in highly perturbed environments [4], where the effects of dynamical model errors are more relevant. Example of these environments are the weak stability boundaries (WSB) in the Earth–Moon system [5], libration-point orbits of the 3-body problem [6], and the orbits around small celestial bodies [7].

These novelties require a stochastic-oriented mission analysis, which elaborates on methods for space flight trajectory optimization under uncertainty. The stochastic optimal control problem [8] can be directly considered, by formulating it through the Bellman equation for discrete-time problems [9], and the Hamilton–Jacobi–Bellman (HJB) equation for continuous-time [10]. Numerical solutions of the HJB equation have been proposed in [11, 12], while locally expanding the Bellman equation around a reference trajectory has brought to differential dynamic programming (DDP) [13], and its generalization, named stochastic DDP [14]. Alternatively, it is possible to deal with the stochastic nature of the problem by employing uncertainty propagation techniques [15]. Although these techniques come from the field of navigation and estimation, they can be used in a stochastic trajectory optimization problem. Indeed, with these techniques it is possible to deterministically assess the uncertainties, thus transforming the stochastic optimization problem into a deterministic, more conventional problem. These methods can be classified as linear, when they involve a linearization of the dynamics with respect to a reference trajectory [16], or nonlinear methods, which are more computationally expensive, but can produce more accurate predictions. In all these methods, unbounded distribution are often considered. However, imposing hard constraints on unbounded stochastic states is not possible. Therefore, constraints are often reformulated in probabilistic terms, by requiring the probability of meeting the constraints to exceed a specified threshold. This approach is known as chance-constrained optimal control [17, 18].

The methodologies for trajectory optimization under uncertainty have been applied in a diverse range of problems. In [19] linear covariance propagation has been used with maneuver execution errors and process noise to optimize the number, location, and magnitude of impulsive correction maneuvers in a trajectory from LEO to a near rectilinear halo orbit (NRHO). The unscented optimal control problem was first considered in [20], where the nonlinear propagation technique of the unscented transformation (UT) [21] was used to handle navigational uncertainties in an open-loop framework. As a further development, the unscented transformation has been used in an hybrid multiple-shooting approach [22, 23], to optimize trajectories while controlling the covariance and abiding to chance-constraints on the maximum thrust. This approach was applied to interplanetary transfers under the effect of navigation errors and process noise in the dynamics. In other works the unscented transformation was combined with stochastic differential dynamic programming for low-thrust trajectory optimization, defining the tube stochastic optimal control problem [24]. Additionally, an hybrid uncertainty propagation method, mixing the unscented transformation with linear covariance methods, was developed in [25], and applied to a small-body global-mapping scenario around asteroid 101955 Bennu, while using chance-constraints to respect scientific requirements. Chance-constraints were also employed in [26], where convex programming was used to solve low-thrust minimum-fuel trajectory optimization under covariance control. To obtain higher order stochastic moments, the polynomial chaos expansion (PCE) [27] was used to develop a general procedure for stochastic optimization under the uncertainty from the initial state and system parameters [28]. In [2], a revised preliminary mission analysis approach, merging a complete navigation analysis inside the optimization phase, was developed by combining PCE with an extension of UT, i.e, the conjugate unscented transformation [29]. The procedure was applied to the optimization of an highly nonlinear transfer from the Moon to an halo orbit. A similarly comprehensive approach, implementing a complete navigation assessment inside the optimization, was developed in [30], by defining the belief optimal control problem, in which the objective function and the constraints depend directly on the uncertainty distributions, rather than the state realizations. This new approach was applied to the fly-by trajectory of the Europa Clipper mission. The differential algebra approach [31] was applied in [32], to inexpensively propagate the dynamics while solving an optimal control problem with uncertain boundary conditions. This approach was also applied to the optimal station-keeping problem on NRHO and quasi-satellite orbits, using an high-order target point approach [33]. A Gaussian mixture model [34] was used for spacecraft maneuver design in [35], to approximate chance-constraints on a non-normal distribution, while state transition tensors [36] were used for the uncertainty propagation of each Gaussian mixand.

Although research on stochastic trajectory optimization has produced different methods to obtain optimal solutions, usually a compromise between accuracy on uncertainty propagation and computational efficiency has to be made. Indeed, linearized methods benefit from fast computations, but may generally lack accuracy for highly nonlinear dynamics or long propagation times. On the contrary, nonlinear methods offer more precision in uncertainty propagation, but require a great amount of samples to be propagated, or need higher-order dynamical expansions that may be complex to

obtain. For these reasons, only a subset of uncertainty sources inside the optimization are often considered, to reduce the computational burden. A sweet spot between accuracy and computational efficiency may be held by the unscented transformation, as it requires the minimum number of samples, called sigma points, to estimate the state mean and covariance in a nonlinear propagation framework. However, the sampling of sigma points relies on the assumption of Gaussian distribution, which may be an oversimplification for complex dynamical systems. The present work proposes a new methodology to solve these issues. In particular, a new method for stochastic trajectory optimization with impulsive guidance is developed. The method considers all the main sources of uncertainty, which are the initial conditions, the maneuvers executions, and the navigation, while process noise in the dynamics is implemented after the optimization. The costs of both open-loop nominal maneuvers and closed-loop correction maneuvers are minimized together, while satisfying stochastic covariance constraints on the final target. The method relies on the unscented transformation to propagate the uncertainties and transcribe the stochastic optimization problem into a deterministic nonlinear programming (NLP) [37] problem, which can be solved through conventional gradient-based optimization techniques. However, the implementation of the unscented transformation improves upon previous research [22–25] by using a continuous propagation map, where trajectories and uncertainties are propagated together from the initial to the final time. As a consequence, no resampling of the sigma points is needed during propagation, which avoids the simplification of assuming a Gaussian distribution at each resampling time, and allows the nonlinear dynamics to modify the distribution freely. Therefore, the use of a continuous nonlinear propagation map improves accuracy while keeping the same number of sigma points. In addition, the focus of the method shifts from the propagation of the first stochastic moments, i.e., the mean and covariance, to the direct propagation of the samples realizations. As a consequence, the method allows propagating a nominal trajectory alongside true trajectories, where the effects of errors are considered. Given the absence of any resampling, each one of these trajectories is continuous, which facilitates direct post-processing applications. Additionally, conventional constraints can be directly imposed on the nominal trajectory, eliminating the need for reformulation as required in the chance-constrained optimal control approach. Eventually, the method allows implementing an optimal guidance strategy for correction maneuvers. This is achieved by letting the guidance matrices be part of the set of optimization variables. This approach is compared to traditional strategies were the guidance matrix is predetermined by a guidance law.

For the first time, a stochastic optimization method is applied to Earth–Moon WSB transfers. These transfers are characterized by a long time of flight, usually between 3 and 4 months, and thus require a computationally efficient uncertainty propagation method. In addition, the highly nonlinear dynamics of these transfers marks a good test for the accuracy of the propagation method. At last, the recent popularity of the WSB transfers for reaching the Moon, makes them interesting candidates for stochastic optimization techniques. The LUMIO CubeSat mission [38, 39] is used as a test case. This mission plans to use a WSB transfer to reach a quasi-halo orbit around the L_2 point, from which the CubeSat will study the meteoroid flux impacting on the lunar far side. The dynamics around the target orbit further

increases the nonlinearity of the transfer, making this mission a good test case for the stochastic optimization method. Moreover, the limited ΔV budget of the mission calls for further optimization of its transfer trajectory, which is achieved through the proposed methodology. Indeed, results show that the new method yields both more fuel-efficient and robust trajectories compared to the traditional sequential approach, where the stochastic analysis is implemented outside the optimization phase. Eventually, results are validated with Monte Carlo simulations, to test the validity of the unscented transformation with the proposed propagation map.

This paper is organized as follows. In Section II the assumptions for the problem are made, the unscented transformation is implemented and the propagation map is defined, the guidance strategies are established, and the final problem is formulated. In Section III the LUMIO mission is introduced, the stochastic optimization problem is implemented, and results are presented and validated with Monte Carlo analyses. In Section IV concluding remarks are made.

II. Methodology

In this section, the method for impulsive trajectory optimization under uncertainty is introduced. The objective is to transform the stochastic problem into a nonlinear programming problem, owing to the unscented transformation. In this way the optimization problem can be solved with conventional gradient-based optimization techniques. To propagate trajectories alongside uncertainties, a continuous propagation map is defined. This shall contain both the propagation of the equations of motion, and the effects of the errors on the trajectory. The objective function of the problem takes into account both the deterministic ΔV, coming from the nominal trajectory, and the stochastic ΔV, given by correction maneuvers. Nominal constraints are considered together with stochastic constraints on the trajectory dispersion.

A. Assumptions

Considering a generic space flight trajectory, the state $\boldsymbol{x} = [\boldsymbol{r}, \boldsymbol{v}]^\top$ collects the position, $\boldsymbol{r}$, and velocity, $\boldsymbol{v}$, vectors at any time. This is discretized in n intervals, $t_0, \dots, t_n$, corresponding to maneuvering epochs. At time t_0, initial conditions are modeled as a Gaussian random variable, $\boldsymbol{x}_0 \sim \mathcal{N}(\overline{\boldsymbol{x}}_0, \boldsymbol{P}_0)$, with mean $\overline{\boldsymbol{x}}_0$ and covariance $\boldsymbol{P}_0 = \frac{1}{3}\text{diag}\left(\sigma_{r,0}^2 \boldsymbol{I}_3, \sigma_{v,0}^2 \boldsymbol{I}_3\right)$, where $\sigma_{r,0}$ and $\sigma_{v,0}$ are the initial position and velocity standard deviations, and $\boldsymbol{I}_3$ is the 3-dimensional identity matrix. At time t_k, for $k = 1, \dots, n$, an open-loop nominal maneuver, $\Delta\boldsymbol{v}_k$, and a closed-loop correction maneuver, $\Delta\boldsymbol{v}_k$, can be applied. Open-loop maneuvers are affected by execution errors, whereas correction maneuvers are affected by navigation errors, through the closed-loop control, while execution errors are deemed negligible. Open-loop maneuvers occur only at times where they are needed, while closed-loop maneuvers are executed at each time t_k, for $k = 1, \dots, n-1$. An example of a possible maneuver schedule is shown in Fig. 1. The set of indexes for which an open-loop maneuver is planned is defined as

$$\mathbb{M} = \{m \in [\![0, n]\!] \mid \exists\, \Delta\boldsymbol{v}_m\} \tag{1}$$

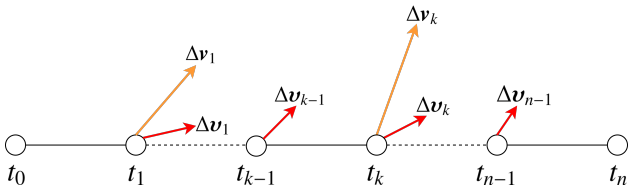

Fig. 1 Example of maneuvers schedule. Orange and red arrows are, respectively, open-loop and closed-loop maneuvers.

An open-loop maneuver at time t_m is modeled as a Gaussian random variable, $\Delta \boldsymbol{v}_m \sim \mathcal{N}\left(\overline{\Delta \boldsymbol{v}}_m, \boldsymbol{P}_{\Delta \boldsymbol{v}_m}\right)$, with mean $\overline{\Delta \boldsymbol{v}}_m$ equal to the nominal impulse, and covariance $\boldsymbol{P}_{\Delta \boldsymbol{v}_m}$. The covariance matrix is determined by a relative error on the thrust magnitude, with standard deviation $\sigma_{\Delta v}$, and an absolute error on the pointing angles, with standard deviation σ_δ. In spherical coordinates the covariance is $\boldsymbol{P}^s_{\Delta \boldsymbol{v}_m} = \text{diag}\left(\sigma^2_{\Delta v} \|\overline{\Delta \boldsymbol{v}}_m\|^2, \sigma^2_\delta, \sigma^2_\delta\right)$, from which the covariance in Cartesian coordinates, $\boldsymbol{P}_{\Delta \boldsymbol{v}_m}$, can be retrieved as

$$\boldsymbol{P}_{\Delta \boldsymbol{v}_m} = \boldsymbol{J}_m \boldsymbol{P}^s_{\Delta \boldsymbol{v}_m} \boldsymbol{J}_m^\top \tag{2}$$

where $\boldsymbol{J}_m$ is the Jacobian of the spherical to Cartesian transformation for the maneuver at time t_m. Regarding navigation errors, no explicit knowledge analysis is performed. Instead, for all maneuvering times a single orbit determination (OD) error is implemented as a Gaussian random variable, $\boldsymbol{\varepsilon}_{OD} \sim \mathcal{N}\left(\overline{\boldsymbol{\varepsilon}}_{OD}, \boldsymbol{P}_{OD}\right)$, with $\overline{\boldsymbol{\varepsilon}}_{OD} = \boldsymbol{0}$ and covariance $\boldsymbol{P}_{OD} = \frac{1}{3}\text{diag}\left(\sigma^2_{r,OD}\boldsymbol{I}_3, \sigma^2_{v,OD}\boldsymbol{I}_3\right)$, where $\sigma_{r,OD}$ and $\sigma_{v,OD}$ are the standard deviations for the orbit determination error, for position and velocity, respectively. Eventually, dynamical model errors are assumed to be negligible, and are not considered inside the optimization. However, they are still considered in the Monte Carlo analyses for the validation phase. Noise in the dynamics is modeled as a Gauss–Markov process [40], $\eta\left(t\right)$, obeying to the Langevin equation [41]:

$$\dot{\eta}\left(t\right) = -\beta\eta\left(t\right) + \omega\left(t\right) \tag{3}$$

where β is the inverse of the correlation time, and ω is a driving white noise with zero mean and standard deviation σ_ω. Operatively, the Gauss–Markov process is implemented in the equations of motion via a discrete random driving sequence, with the so-called statistics-preserving model [42]:

$$\eta(t) = \eta_0 e^{-l\beta\,\delta t} e^{-\beta(t-t_l)} + \sum_{i=0}^{l-1}\left(\omega_i\sqrt{\frac{1}{2\beta}\left(1-e^{-2\beta\,\delta t}\right)}e^{-\beta(t-t_{i+1})}\right) + \omega_l\sqrt{\frac{1}{2\beta}\left(1-e^{-2\beta(t-t_l)}\right)} \tag{4}$$

where, independently of the previous time discretization, time has been divided in l steps of duration δt, so that for each time interval $[t_i, t_{i+1}]$, the corresponding noise, ω_i, is assumed to be constant. With this formulation the standard deviation of the driving noise can be computed as $\sigma_\omega = \sqrt{2\beta}\sigma_{GM}$, with σ_{GM} being the standard deviation of the Gauss–Markov process itself.

B. Trajectory Propagation Under Uncertainty

All sources of uncertainty are collected inside a single N-dimensional vector of Gaussian variables, $\boldsymbol{\mathcal{X}}_0$, defined as

$$\begin{aligned} \boldsymbol{\mathcal{X}}_0 \sim \mathcal{N}\left(\overline{\boldsymbol{\mathcal{X}}}_0, \boldsymbol{\mathcal{P}}_0\right) &= \left[\boldsymbol{x}_0, \Delta\boldsymbol{v}_{\mathbb{M}}, \boldsymbol{\varepsilon}_{OD}\right]^\top \\ \overline{\boldsymbol{\mathcal{X}}}_0 &= \left[\overline{\boldsymbol{x}}_0, \overline{\Delta\boldsymbol{v}}_{\mathbb{M}}, \overline{\boldsymbol{\varepsilon}}_{OD}\right]^\top \\ \boldsymbol{\mathcal{P}}_0 &= \operatorname{diag}\left(\boldsymbol{P}_0, \boldsymbol{P}_{\Delta\boldsymbol{v}_{\mathbb{M}}}, \boldsymbol{P}_{OD}\right) \end{aligned} \tag{5}$$

where $\Delta\boldsymbol{v}_{\mathbb{M}}$ indicates the vector containing each $\Delta\boldsymbol{v}_m$, and, similarly, $\boldsymbol{P}_{\Delta\boldsymbol{v}_{\mathbb{M}}}$ is the block-diagonal matrix of each open-loop maneuver covariance matrix. From this initial distribution, a set of $2N+1$ initial *sigma points* is created: $\boldsymbol{\mathcal{X}}_0^j \in \{\boldsymbol{\mathcal{X}}_0^0, \ldots, \boldsymbol{\mathcal{X}}_0^{2N}\}$, where the superscript j indicates the sigma point number. These are computed as [21]

$$\boldsymbol{\mathcal{X}}_0^j = \left\{ \begin{array}{ll} \overline{\boldsymbol{\mathcal{X}}}_0 & \text{for } j = 0 \\ \overline{\boldsymbol{\mathcal{X}}}_0 + \left[\sqrt{(N+\lambda)\,\boldsymbol{\mathcal{P}}_0}\right]_j & \text{for } j = 1 \rightarrow N \\ \overline{\boldsymbol{\mathcal{X}}}_0 - \left[\sqrt{(N+\lambda)\,\boldsymbol{\mathcal{P}}_0}\right]_{j-N} & \text{for } j = N+1 \rightarrow 2N \end{array} \right\} \tag{6}$$

where $[\cdot]_i$ is the operator that extracts the i-th column vector of a matrix, and λ is a scaling parameter that is assumed zero in this work.

The propagation of the sigma points at later time t_k is ensured by a nonlinear mapping, indicated with $\mathcal{F}$. The requirements on $\mathcal{F}$ are the following:

1) The full sigma point vector, $\boldsymbol{\mathcal{X}}_k^j$, should contain the sigma points for each uncertainty: $\boldsymbol{\mathcal{X}}_k^j = \left[\boldsymbol{x}_k^j, \Delta\boldsymbol{v}_{\mathbb{M}}^j, \boldsymbol{\varepsilon}_{OD}^j\right]^\top$.
2) The sigma points of the state, $\boldsymbol{x}_k^j$, should be the result of the propagation of the initial conditions through the equations of motion, and of the effects of the uncertain maneuvers.
3) The sigma points of each open-loop maneuver, $\Delta\boldsymbol{v}_m^j$, and of the navigation error, $\boldsymbol{\varepsilon}_{OD}^j$, do not propagate as they are constant in time. However, their effects shall be considered at each appropriate time.
4) The evolution of the central sigma point, $\boldsymbol{x}_0^j$, should represent the nominal trajectory, which is clear of any error.
5) The propagation should be continuous between initial time, t_0, and final time, t_n, without any resampling of sigma points at each maneuvering time, t_k.

Considering the time interval between two consecutive maneuvers, $[t_{k-1}, t_k]$, the nonlinear mapping $\mathcal{F} : \boldsymbol{\mathcal{X}}_{k-1}^j \mapsto \boldsymbol{\mathcal{X}}_k^j$ is composed of 3 sub-maps:

$$\boldsymbol{\mathcal{X}}_k^j = \mathcal{F}\left(\boldsymbol{\mathcal{X}}_{k-1}^j\right) = \begin{bmatrix} \mathcal{F}_{\boldsymbol{x}}\left(\boldsymbol{\mathcal{X}}_{k-1}^j\right) \\ \mathcal{I}_{\Delta\boldsymbol{v}}\left(\boldsymbol{\mathcal{X}}_{k-1}^j\right) \\ \mathcal{I}_{\boldsymbol{\varepsilon}}\left(\boldsymbol{\mathcal{X}}_{k-1}^j\right) \end{bmatrix} \tag{7}$$

where $\mathcal{I}_{\Delta \boldsymbol{v}}$ and $\mathcal{I}_{\boldsymbol{\varepsilon}}$ are the identity maps that simply output $\Delta \boldsymbol{v}_{\mathbb{M}}^{j}$ and $\boldsymbol{\varepsilon}_{OD}^{j}$ at each time t_k, while the sub-map $\mathcal{F}_{\boldsymbol{x}}$ is recursively defined as

$$\boldsymbol{x}_k^j = \mathcal{F}_{\boldsymbol{x}}\left(\boldsymbol{x}_{k-1}^j\right) = \left\{ \begin{array}{ll} \boldsymbol{\varphi}\left(\boldsymbol{x}_{k-1}^j, t_{k-1}, t_k\right) & \text{if } j = 0 \wedge k \notin \mathbb{M} \\ \boldsymbol{\varphi}\left(\boldsymbol{x}_{k-1}^j, t_{k-1}, t_k\right) + \left[\boldsymbol{0}, \Delta \boldsymbol{v}_k^j\right]^{\top} & \text{if } j = 0 \wedge k \in \mathbb{M} \\ \boldsymbol{\varphi}\left(\boldsymbol{x}_{k-1}^j, t_{k-1}, t_k\right) + \left[\boldsymbol{0}, \Delta \boldsymbol{v}_k^j\right]^{\top} & \text{if } j \neq 0 \wedge k \notin \mathbb{M} \\ \boldsymbol{\varphi}\left(\boldsymbol{x}_{k-1}^j, t_{k-1}, t_k\right) + \left[\boldsymbol{0}, \Delta \boldsymbol{v}_k^j\right]^{\top} + \left[\boldsymbol{0}, \Delta \boldsymbol{v}_k^j\right]^{\top} & \text{if } j \neq 0 \wedge k \in \mathbb{M} \end{array} \right\} \tag{8}$$

where $\boldsymbol{\varphi}\left(\boldsymbol{x}_{k-1}^j, t_{k-1}, t_k\right)$ is the *flow* of the equations of motion, out of $\boldsymbol{x}_{k-1}^j$, and from t_{k-1} to t_k. The correction maneuver, $\Delta \boldsymbol{v}_k^j$, related to the j-th sigma point at time t_k, is computed with a closed-loop control (Section II.C), and following a prescribed guidance strategy (Section II.D). As stated in the assumption, this maneuver is affected by the navigation error, through its realization $\boldsymbol{\varepsilon}_{OD}^j$. The propagation map $\mathcal{F}$ is defined recursively from t_k to t_{k+1}, but it is continuously applied from t_0 to t_n. A schematic representation of the propagation is shown in Fig. 2. It is important to highlight that the evolution of the central sigma point represents the nominal trajectory. Indeed, $\boldsymbol{x}_k^0$ derives from the propagation of the nominal initial conditions, $\boldsymbol{x}_0^0$, and of the effects of the nominal open-loop maneuvers, $\Delta \boldsymbol{v}_m^0$, while no closed-loop maneuvers, affected by the navigation error, are considered for correction. On the contrary, the evolution of the external sigma points represent the *true* dispersed trajectories, which contain all sources of errors and are a realistic simulation of space flight under its uncertainties.

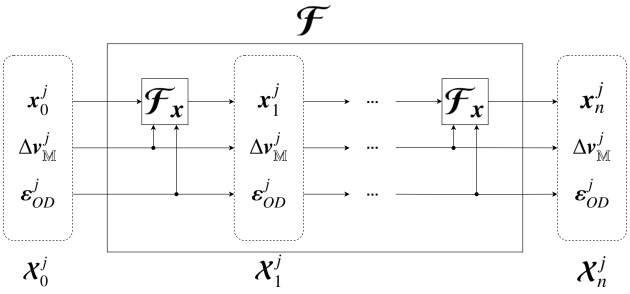

Fig. 2 Propagation scheme for a generic sigma point.

Finally, the mean value and covariance matrix of the states at any time t_k are computed with the unscented transformation sample mean and covariance formulas [21]:

$$\overline{\boldsymbol{x}}_k = \sum_{j=0}^{2N} w^j \boldsymbol{x}_k^j \tag{9}$$

$$\boldsymbol{P}_k = \sum_{j=0}^{2N} w^j \left(\boldsymbol{x}_k^j - \overline{\boldsymbol{x}}_k\right)\left(\boldsymbol{x}_k^j - \overline{\boldsymbol{x}}_k\right)^{\top} \tag{10}$$

where the weights are $w^0 = \dfrac{\lambda}{N+\lambda}$, and $w^j = \dfrac{1}{2\,(N+\lambda)}$, for $j = 1 \rightarrow 2N$.

The procedure defined in this section to propagate the trajectory under uncertainty is similar, in principle, to other methods relying on the unscented transformation, such as the ones in [22–25]. However, the methodology developed here introduces key innovations that offer practical advantages for mission analysis. Unlike previous approaches, where sigma points were resampled at each time t_k from the sample mean and covariance, the method developed in this work continuously propagates sigma points with the map $\mathcal{F}$ up to the final time t_n, eliminating the need for intermediate resampling. In other words, the procedure developed here directly works on the realizations of the trajectory, represented by the sigma points, rather than focusing on the propagation of the stochastic moments of the trajectory, i.e., the mean and covariance. This results in a less simplified and more accurate implementation of the uncertainty propagation. Indeed, resampling sigma points assumes that the distribution remains normal [22–25], which is a simplification. By avoiding resampling, the nonlinear map $\mathcal{F}$ is allowed to naturally evolve the distribution in a non-normal way. Then, at each t_k, the mean and covariance can still be estimated from the sample formulas in Eqs. (9) and (10). The advantage of this implementation is that working with realizations instead of stochastic moments enables the computation of continuous trajectories and provides a clear distinction between nominal and dispersed trajectories. The data coming from these continuous trajectories can be directly used in post-processing applications, as for example creating a kernel of the nominal trajectory. On the contrary, the mean trajectory would exhibit discontinuities due to sigma points resampling, necessitating additional processing before further use.

C. Closed-Loop Control

As the effects of uncertainties accumulate in time, and as the dispersion increases through the nonlinear equations of motion, control is needed to make the spacecraft achieve its final target. In this work, closed-loop control is used to steer the dispersed trajectories towards the nominal one. In particular, closed-loop correction maneuvers are computed following the Markov control policy [43], i.e., the control depends only on the current state, rather than its entire history. Thus, each correction maneuver, $\Delta\boldsymbol{v}_k^j$, is given by the product of a guidance matrix, $\boldsymbol{G}_k$, and a closed-loop error, $\Delta\hat{\boldsymbol{x}}_k^j$, defined, for each sigma point, as the difference between the estimate of the true state, $\hat{\boldsymbol{x}}_k^j$, and the nominal one, $\boldsymbol{x}_k^0$. Therefore, the closed-loop maneuver is

$$\Delta\boldsymbol{v}_k^j = \boldsymbol{G}_k \Delta\hat{\boldsymbol{x}}_k^j = \boldsymbol{G}_k \left(\hat{\boldsymbol{x}}_k^j - \boldsymbol{x}_k^0\right) \tag{11}$$

The matrix $\boldsymbol{G}_k$ is computed according to a selected guidance strategy; see Section II.D. The estimated state comes, instead, from the orbit determination procedure. In particular, a cut-off (CO) time, Δt_{CO}, is established before maneuvers, so that the final time of the k-th orbit determination, $t_{OD,k}$, is $t_{OD,k} = t_k - \Delta t_{CO}$. As indicated in the assumptions, the

result of the orbit determination, $\boldsymbol{x}^j_{OD,k}$, is given by the true state plus the navigation error:

$$\boldsymbol{x}^j_{OD,k} = \boldsymbol{\varphi}\left(\boldsymbol{x}^j_{k-1}, t_{k-1}, t_{OD,k}\right) + \boldsymbol{\varepsilon}^j_{OD} \tag{12}$$

Finally, the estimated state, $\hat{\boldsymbol{x}}^j_k$, is the propagation through the cut-off time of the orbit determination result, plus the open-loop nominal maneuver, if any:

$$\begin{aligned} \hat{\boldsymbol{x}}^j_k &= \boldsymbol{\varphi}\left(\boldsymbol{x}^j_{OD,k}, t_{OD,k}, t_k\right) + \left[\boldsymbol{0}, \Delta\boldsymbol{v}^0_k\right]^\top && \text{if } k \in \mathbb{M} \\ \hat{\boldsymbol{x}}^j_k &= \boldsymbol{\varphi}\left(\boldsymbol{x}^j_{OD,k}, t_{OD,k}, t_k\right) && \text{if } k \notin \mathbb{M} \end{aligned} \tag{13}$$

where the nominal maneuver, $\Delta\boldsymbol{v}^0_k$, is considered as it is the expected execution of the maneuver, which differs from its real execution, $\Delta\boldsymbol{v}^j_k$. This reflects the fact that the navigation process, which ends at time $t_{OD,k}$, has no information on the real execution of the open-loop maneuver, which happens at time t_k, after the cut-off period, Δt_{CO}. In this way, the closed-loop maneuver, $\Delta\boldsymbol{v}^j_k$, does not correct the error due to the execution of the simultaneous open-loop maneuver, $\Delta\boldsymbol{v}^j_k$, which would be an unrealistic scenario. Instead, the execution error will be corrected by the following closed-loop maneuvers, at later times.

To clarify the difference between the nominal, true, and estimated trajectories, and the computation of closed-loop correction maneuvers, a schematic representation of the propagation process between t_{k-1} and t_k is shown in Fig. 3. Here, the black line represents the nominal trajectory, obtained through the propagation of the central sigma point. Similarly, the orange line is a possible true trajectory, represented by the propagation of the j-th sigma point, for $j \neq 0$. The red trajectory is its estimate after the OD process, which is highlighted in gray. The black arrow is the nominal open-loop maneuver, the orange one is the true open-loop maneuver, affected by the execution error, while the red one is the closed-loop maneuver. It is important to highlight that the closed-loop maneuver is computed for the estimated trajectory, as it is shown in Eq. (11), but it is executed on the true one. Lastly, the orange dots are the true states after the execution of all maneuvers, while the red dot is the estimated state after the execution of the open-loop maneuver only, which, as explained, is estimated to be the nominal one.

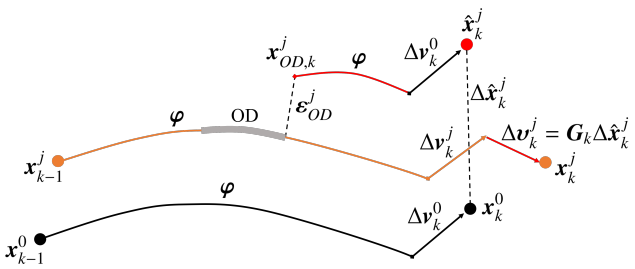

Fig. 3 Trajectory propagation process of the nominal, true, and estimated trajectories.

D. Guidance Strategy

To achieve the desired control, the matrix $\boldsymbol{G}_k$ in Eq. (11) should be computed with a proper guidance strategy. In this work two different strategies are implemented: the *differential guidance* (DG) and the *optimal guidance* (OG).

The differential guidance [44] is a commonly used type of guidance for space flight applications. The main idea behind this guidance is to compute correction maneuvers to linearly cancel future deviations from the reference trajectory. To predict future deviations from the reference state $\boldsymbol{x}_0$, the state transition matrix (STM) $\boldsymbol{\Phi}$, defined as $\boldsymbol{\Phi}\left(\boldsymbol{x}_0, t_0, t\right) = \dfrac{\partial \boldsymbol{\varphi}\left(\boldsymbol{x}_0, t_0, t\right)}{\partial \boldsymbol{x}_0}$, is used. Considering an initial deviation from the reference, $\delta\boldsymbol{x}_0$, the future deviation, $\delta\boldsymbol{x}\left(t\right)$, is linearly approximated as $\delta\boldsymbol{x}\left(t\right) = \boldsymbol{\Phi}\left(\boldsymbol{x}_0, t_0, t\right)\delta\boldsymbol{x}_0$. Therefore, considering the time interval $[t_k, t_{k+1}]$, the differential guidance is the 2-impulse solution of

$$[\delta\boldsymbol{r}_{k+1}, \delta\boldsymbol{v}_{k+1}]^\top = \boldsymbol{\Phi}\left(\boldsymbol{x}_k, t_k, t_{k+1}\right)\left\{[\delta\boldsymbol{r}_k, \delta\boldsymbol{v}_k]^\top + [\boldsymbol{0}, \Delta\boldsymbol{v}_k]^\top\right\} + [\boldsymbol{0}, \Delta\boldsymbol{v}_{k+1}]^\top = \boldsymbol{0} \tag{14}$$

However, it is standard practice to neglect the second impulse, $\Delta\boldsymbol{v}_{k+1}$, in Eq. (14), as at t_{k+1} another maneuver can be computed in a receding-horizon approach. Therefore, Eq. (14) can be solved only for $\Delta\boldsymbol{v}_k$, by minimizing the weighted norm of the final deviation, $\|\delta\boldsymbol{r}_{k+1}\|^2 + q\|\delta\boldsymbol{v}_{k+1}\|^2$, where q is a weighting factor. This brings to the minimum solution [44]

$$\Delta\boldsymbol{v}_k = -\left(\boldsymbol{\Phi}_{rv}^\top\boldsymbol{\Phi}_{rv} + q\boldsymbol{\Phi}_{vv}^\top\boldsymbol{\Phi}_{vv}\right)^{-1}\left(\boldsymbol{\Phi}_{rv}^\top\boldsymbol{\Phi}_{rr} + q\boldsymbol{\Phi}_{vv}^\top\boldsymbol{\Phi}_{vr}\right)\delta\boldsymbol{r}_k - \delta\boldsymbol{v}_k \tag{15}$$

where $\boldsymbol{\Phi}_{rr}$, $\boldsymbol{\Phi}_{rv}$, $\boldsymbol{\Phi}_{vr}$, and $\boldsymbol{\Phi}_{vv}$ are the 3-by-3 STM sub-matrices defined by taking the rows and columns related to the position, r, and the velocity, v. Finally, by applying the differential guidance on Eq. (11), with the reference trajectory as the nominal one, $\boldsymbol{\Phi} = \boldsymbol{\Phi}\left(\boldsymbol{x}_k^0, t_k, t_{k+1}\right)$, and the initial deviation as $\hat{\boldsymbol{x}}_k^j - \boldsymbol{x}_k^0$, the resulting differential guidance matrix, $\boldsymbol{G}_k$, is

$$\boldsymbol{G}_k = -\left[\left(\boldsymbol{\Phi}_{rv}^\top\boldsymbol{\Phi}_{rv} + q\boldsymbol{\Phi}_{vv}^\top\boldsymbol{\Phi}_{vv}\right)^{-1}\left(\boldsymbol{\Phi}_{rv}^\top\boldsymbol{\Phi}_{rr} + q\boldsymbol{\Phi}_{vv}^\top\boldsymbol{\Phi}_{vr}\right),\ \boldsymbol{I}_3\right] \tag{16}$$

Although the differential guidance works exactly only in linear dynamics, it can give good results even in nonlinear environments, provided that the time between consecutive correction maneuvers is short. However, a more gradual and predictive control could perform better than simply minimizing the future deviations sequentially. For this reason an optimal guidance is considered, where the elements of $\boldsymbol{G}_k$ are left completely free to vary during an optimization process. While the optimizer tries to minimize an objective function accounting for the cost of the correction maneuvers, each guidance matrix should change accordingly. Of course, this type of guidance can be used only if a stochastic optimization is to be performed, otherwise no knowledge on the elements of $\boldsymbol{G}_k$ can be attained. Moreover, there is no guarantee that this type of guidance will work, and the solution may be application-dependent. Nonetheless, starting from a good initial guess, such as the differential guidance itself, might ease the solution of the optimal guidance problem.

E. Statement of the Problem

The stochastic optimization problem is formulated as a NLP problem. The NLP vector, $\boldsymbol{y}$, contains all the optimization variables, which are the nominal initial condition, the open-loop maneuvers, the maneuvers times, and the guidance matrices if the optimal guidance is considered. Thus:

$$\boldsymbol{y} = \left\{ \begin{array}{ll} \left[\boldsymbol{x}_0^0, \Delta\boldsymbol{v}_{\mathbb{M}}, \boldsymbol{t}\right]^\top & \text{if DG} \\ \left[\boldsymbol{x}_0^0, \Delta\boldsymbol{v}_{\mathbb{M}}, \boldsymbol{g}, \boldsymbol{t}\right]^\top & \text{if OG} \end{array} \right\} \tag{17}$$

where $\boldsymbol{g} = \left[\text{vect}\left(\boldsymbol{G}_1\right), \ldots, \text{vect}\left(\boldsymbol{G}_{n-1}\right)\right]^\top$ is the vector containing all the vectorized optimal guidance matrices, and $\boldsymbol{t} = \left[t_0, \ldots, t_n\right]^\top$ is the vector with all the maneuvering times. In the differential guidance case, no variables on the closed-loop control are needed as the guidance matrices are completely defined by the nominal trajectory, as it can be seen in Eq. (16). The objective function takes into account both the deterministic cost, ΔV_{det}, and the stochastic cost, ΔV_{sto}: their sum defines the total cost, ΔV_{tot}. Thus:

$$J\left(\boldsymbol{y}\right) := \Delta V_{tot} = \Delta V_{det} + \Delta V_{sto} \tag{18}$$

In particular, ΔV_{det} is defined as the sum of the norm of each nominal open-loop impulse, while ΔV_{sto} is defined as the 3-sigma value of the sum of the norm of each closed-loop impulse:

$$\Delta V_{det} = \sum_{m \in \mathbb{M}} \|\Delta\boldsymbol{v}_m^0\| \tag{19}$$

$$\Delta V_{sto} = \overline{\Delta\upsilon} + 3\sigma_{\Delta\upsilon} \tag{20}$$

where the mean value, $\overline{\Delta\upsilon}$, and the standard deviation, $\sigma_{\Delta\upsilon}$, are computed with the weighted sample mean and covariance formulas:

$$\overline{\Delta\upsilon} = \sum_{j=0}^{2N} w^j \left(\sum_{k=1}^{n-1} \|\Delta\boldsymbol{v}_k^j\| \right) \tag{21}$$

$$\sigma_{\Delta\upsilon} = \sqrt{\sum_{j=0}^{2N} w^j \left(\sum_{k=1}^{n-1} \|\Delta\boldsymbol{v}_k^j\| - \overline{\Delta\upsilon} \right)^2} \tag{22}$$

Eventually, constraints are implemented. By enabling the definition of a nominal trajectory, the method allows the application of conventional mission constraints without requiring a chance-constrained approach. In particular, initial, $\boldsymbol{\Psi}_0\left(\boldsymbol{x}_0^0, t_0\right)$, and final, $\boldsymbol{\Psi}_n\left(\boldsymbol{x}_n^0, t_n\right)$, boundary constraints can be implemented. Boundary conditions are collected in the

vector of equality constraints, $\boldsymbol{c}_{eq}$, defined as

$$\boldsymbol{c}_{eq}\left(\boldsymbol{y}\right) = \left\{ \begin{array}{c} \boldsymbol{\Psi}_0\left(\boldsymbol{x}_0^0, t_0\right) \\ \boldsymbol{\Psi}_n\left(\boldsymbol{x}_n^0, t_n\right) \\ \boldsymbol{c}\left(\boldsymbol{y}\right) \end{array} \right\} = \boldsymbol{0} \tag{23}$$

where $\boldsymbol{c}$ indicates a generic set of additional constraints that are application-dependent. Similarly, nominal inequality constraints depend on the specific optimization problem that is to be solved. They are generically collected in the vector $\boldsymbol{c}_{in}$, defined as

$$\boldsymbol{c}_{in}\left(\boldsymbol{y}\right) \leq \boldsymbol{0} \tag{24}$$

Additionally, some constraints of stochastic nature can be enforced as well. Indeed, without any stochastic constraints, the minimization of the objective function would bring to small or null correction maneuvers, causing huge dispersion on the trajectory. This should be avoided in mission analysis, because the aim is to reach the final target with high probability. To achieve this, the final covariance matrix, $\boldsymbol{P}_n$, computed according to Eq. (10), is constrained. In particular, upper boundaries are imposed on the trace of the 3-by-3 sub-matrices, $\boldsymbol{P}_{rr,n}$ and $\boldsymbol{P}_{vv,n}$, related to position and velocity, respectively. Thus, the stochastic constraints, $\boldsymbol{c}_{sto}$, are defined as

$$\boldsymbol{c}_{sto}\left(\boldsymbol{y}\right) = \left\{ \begin{array}{c} \mathrm{tr}\left(\boldsymbol{P}_{rr,n}\right) - \tilde{\sigma}_{r,n}^2 \\ \mathrm{tr}\left(\boldsymbol{P}_{vv,n}\right) - \tilde{\sigma}_{v,n}^2 \end{array} \right\} \leq \boldsymbol{0} \tag{25}$$

where $\mathrm{tr}\left(\cdot\right)$ is the trace operator, and $\tilde{\sigma}_{r,n}$ and $\tilde{\sigma}_{v,n}$ are the standard deviation upper boundaries for position and velocity. All in all, the stochastic optimization problem is formulated as

$$\min_{\boldsymbol{y}} \ \text{Eq. (18)} \ \text{ s.t. } \left\{ \begin{array}{c} \text{Eq. (23)} \\ \text{Eq. (24)} \\ \text{Eq. (25)} \end{array} \right\} \tag{26}$$

III. Case Study: LUMIO Weak Stability Boundary Transfers

LUMIO, which stands for LUnar Meteoroid Impacts Observer [38], is a 12U CubeSat that is planned to fly on a quasi-halo orbit around the Earth–Moon L_2 point. From this position, LUMIO will observe, quantify, and characterize the meteoroids flux on the lunar far side, by detecting their impact light flashes. Currently, the mission is expected to launch in 2027. The operational orbit for the mission is a southern quasi-halo orbit around L_2, stemming from an ideal

halo with a Jacobi constant equal to 3.09 [45]. To reach this target, an Earth–Moon weak stability boundary transfer [5] is exploited. A comprehensive review of the methodologies and results of the WSB trajectory design and optimization for the LUMIO mission can be found in [39], where the results of the mission analysis for phase B are shown. The choice of this mission as a case study is motivated by the nonlinearity of the WSB transfer and target orbit, which makes a good test of the effectiveness and accuracy of the proposed methodology. In addition, LUMIO is a CubeSat and its ΔV budget is tight, which means that any possible saving in fuel may be relevant.

The LUMIO mission analysis has followed a sequential approach for the design of the WSB transfer trajectory: first, a nominal trajectory is designed and optimized, and, then, a navigation assessment is performed. Along the transfer, open-loop maneuvers consist in deep-space maneuvers (DSMs) for the intermediate impulses, and the halo insertion maneuver (HIM) at final time. Their number, direction, magnitude, and placement in time is the result of the deterministic optimization process. Closed-loop maneuvers are, instead, referred to as trajectory correction maneuvers (TCMs). Following a navigation assessment, a TCM every 10 days is considered on average. The differential guidance is used to compute each TCM direction and magnitude. A schematic representation of the LUMIO WSB transfer trajectory, together with the operative orbit and end-of-life trajectory, is reported in Fig. 4.

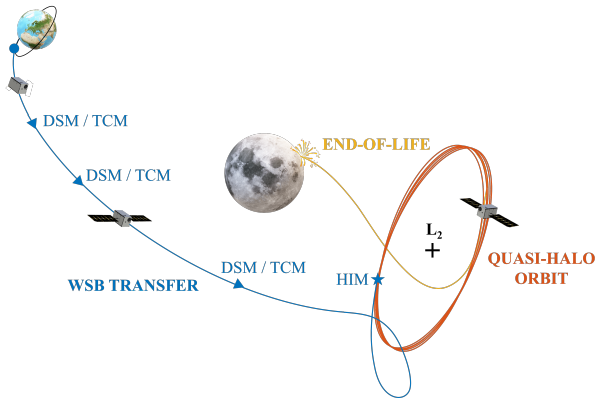

Fig. 4 LUMIO trajectory scheme. The transfer trajectory and maneuvering times are in blue. The operative orbit is in red, while the end-of-life trajectory is in yellow.

In this work, the results of the sequential approach for the optimization of the WSB transfer trajectory will be used as initial guesses for the stochastic optimization problem. In particular, the general problem presented in Eq. (26) is

implemented in the case of LUMIO as

$$\min_{\boldsymbol{y}} \; J(\boldsymbol{y}) = \Delta V_{det} + \Delta V_{sto} \;\; \text{s.t.} \left\{ \begin{array}{c} \boldsymbol{x}_n^0 = \boldsymbol{x}_{qh}(t_n) \\ \text{tr}\left(\boldsymbol{P}_{rr,n}\right) \leq \tilde{\sigma}_{r,n}^2 \\ \text{tr}\left(\boldsymbol{P}_{vv,n}\right) \leq \tilde{\sigma}_{v,n}^2 \\ t_0 = \tilde{t}_0 \\ t_1 \geq t_0 + \Delta t_{com} \\ t_k \geq t_{k-1} + \Delta t_M \quad \text{for } k = 2 \rightarrow n \end{array} \right\} \tag{27}$$

where: the final nominal state, $\boldsymbol{x}_n^0$, is constrained to be on the quasi-halo target orbit, $\boldsymbol{x}_{qh}$, at final time t_n; the initial time, t_0, is constrained to be the epoch, $\tilde{t}_0$, of LUMIO release from the main spacecraft or final launcher stage, which happens 12 hours after the launcher trans lunar injection (TLI) burn; the first maneuvering time, t_1, shall happen after the commissioning of the spacecraft, which lasts $\Delta t_{com} = 6.5$ days; the next maneuvering times, t_k, are at least $\Delta t_M = 3$ days apart from each other, to allow 1 day of orbit determination and 2 days of cut-off time. The time schedule during the transfer is graphically reported in Fig. 5, for clarity. Additionally, no initial boundary constraint is implemented, as the launching conditions for LUMIO are fixed and implicitly satisfied in the propagation map. For the same reason, the NLP vector, $\boldsymbol{y}$, defined according to Eq. (17), does not include the nominal initial state $\boldsymbol{x}_0^0$. The objective function, J, is defined as per Eqs. (18–22). All the relevant data on the uncertain variables are reported in Table 1. In particular, the initial position and velocity dispersion are due to LUMIO release on the post-TLI trajectory. The errors on maneuvers execution come from the choice of the propulsion system, while the navigation error is a representative value coming from the knowledge analysis performed during the navigation assessment for phase B. Lastly, the final covariance constraints are chosen as conventional values to limit the initial dispersion on the quasi-halo orbit, which results in lower station-keeping costs.

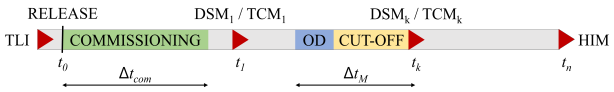

Fig. 5 Time schedule during transfer. The orbit determination and cut-off time intervals are repeated before each maneuver.

The dynamical model for LUMIO is the roto-pulsating restricted n-body problem (RPRnBP) [46]. This is an ephemeris-based model of the solar system, written as an extension of the circular restricted 3-body problem (CR3BP) [47]. Similarly to the CR3BP, the reference frame in the RPRnBP rotates with the primaries, P_1 and P_2, which, in this case, are the Earth and the Moon. In addition, as the motion of the primaries is dictated by the ephemeris, a pulsation affects the reference frame, due to the distance between the primaries changing periodically in time. The roto-pulsating

Table 1 Data used for the stochastic optimization of LUMIO trajectories.

Name	Symbol	Value
Initial Position Dispersion	$\sigma_{r,0}$	100 km
Initial Velocity Dispersion	$\sigma_{r,0}$	5 cm/s
Maneuver Magnitude Error	$\sigma_{\Delta v}$	2%
Maneuver Pointing Angle Error	σ_{δ}	1.5 deg
Position Navigation Error	$\sigma_{r,OD}$	0.1 km
Velocity Navigation Error	$\sigma_{r,OD}$	0.5 mm/s
Final Position Covariance Constraint	$\tilde{\sigma}_{r,n}$	1 km
Final Velocity Covariance Constraint	$\tilde{\sigma}_{r,n}$	1 cm/s

reference frame has the origin on the Earth–Moon barycenter, the x-axis that goes from the Earth to the Moon, the z-axis aligned with their angular momentum, and the y-axis that completes the right-hand frame. A time-dependent conversion from the inertial frame [48] is used to build the roto-pulsating frame. Then, using the Lagrangian formalism and a normalization similar to the CR3BP, the equations of motion can be obtained as [49]

$$\begin{aligned}\boldsymbol{r}'' = &-\frac{2}{n}\left(\frac{\dot{k}}{k}\boldsymbol{I}_3 + \boldsymbol{C}^\top\dot{\boldsymbol{C}}\right)\boldsymbol{r}' - \frac{1}{n^2}\left[\left(\frac{\ddot{k}}{k}\boldsymbol{I}_3 + 2\frac{\dot{k}}{k}\boldsymbol{C}^\top\dot{\boldsymbol{C}} + \boldsymbol{C}^\top\ddot{\boldsymbol{C}}\right)\boldsymbol{r} + \frac{1}{k}\boldsymbol{C}^\top\ddot{\boldsymbol{b}}\right] \\ &+ G\frac{m_1+m_2}{n^2k^3}\left[(1-\mu)\,\frac{\boldsymbol{r}-\boldsymbol{r}_1}{\|\boldsymbol{r}-\boldsymbol{r}_1\|^3} + \mu\frac{\boldsymbol{r}-\boldsymbol{r}_2}{\|\boldsymbol{r}-\boldsymbol{r}_2\|^3} + \sum_j \hat{\mu}_j\frac{\boldsymbol{r}-\boldsymbol{r}_j}{\|\boldsymbol{r}-\boldsymbol{r}_j\|^3}\right] + \boldsymbol{a}_{SRP}\end{aligned} \tag{28}$$

where: the symbols ($'$) and ($\dot{}$) indicate derivatives with respect to the non-dimensional and dimensional time, respectively; $\boldsymbol{r}$, $\boldsymbol{r}_1$, $\boldsymbol{r}_2$, and $\boldsymbol{r}_j$ are the position vectors of the spacecraft, the primaries, and the remaining j-th body of the solar system, in the roto-pulsating frame; n is the mean motion of the primaries, whose value in the case of the Earth–Moon system is $2.6653 \cdot 10^{-6}$ s^{-1}; k is the instantaneous distance between the primaries; $\boldsymbol{C}$ is the rotation matrix between the inertial frame centered on the solar system barycenter and the roto-pulsating frame; $\boldsymbol{I}_3$ is the 3-by-3 identity matrix; $\boldsymbol{b}$ is the position vector of the primaries barycenter in the inertial frame; G is the gravitational constant; m_1 and m_2 are the masses of the primaries; $\mu = \frac{m_2}{m_1+m_2}$ is the mass fraction; $\hat{\mu}_j = \frac{m_j}{m_1+m_2}$; $\boldsymbol{a}_{SRP}$ is the normalized acceleration due to solar radiation pressure (SRP). This is modeled using the cannonball model:

$$\boldsymbol{a}_{SRP} = \frac{1}{kn^2}\frac{c_r A P_0}{m}\frac{d_0^2}{d^2}\frac{\boldsymbol{r}-\boldsymbol{r}_S}{\|\boldsymbol{r}-\boldsymbol{r}_S\|} \tag{29}$$

where $\frac{1}{kn^2}$ is the normalization coefficient, $c_r = 1.3$ is the reflectivity coefficient of the spacecraft, $A = 0.23$ m^2 is the illuminated area of the spacecraft, $m = 28.4$ kg is the spacecraft mass, $P_0 = 4.573$ μPa is the constant reference pressure at a distance $d_0 = 1$ AU, while d is the current distance from the Sun, whose position vector in the roto-pulsating frame is $\boldsymbol{r}_S$. When integrating the equations of motion, the position of the celestial bodies are given by the JPL ephemerides

DE432 [50], which are retrieved with the SPICE toolkit [51, 52]. Similarly, the gravitational constant, G, and the mass, m_j, of each body of the solar system are also provided by the SPICE toolkit.

A. Results

A step-by-step procedure is adopted to find the results: first, the stochastic optimization problem with the differential guidance (DG) is considered, starting from the results of the sequential approach, performed during LUMIO phase B; afterward, the optimal guidance (OG) problem is solved, using the DG solutions as initial guesses. In particular, results for 5 different WSB trajectories are reported, in both guidance cases. These trajectories are a subset of the 52 weekly WSB transfers computed in [39] for the year 2027. As such, trajectories are identified with the number of the week in which the transfer sets off. In this work, trajectories with IDs #02, #11, #20, #43, and #48, are selected. This selection assures that the transfers are distributed along the whole year, to filter out any possible epoch dependence on the results. In addition, this selection considers the two possible types of WSB transfers, i.e., the transfers with the apogee in the second or fourth quadrant of the Sun–Earth rotating frame [53]. Indeed, trajectory #02 and #48 belong to the fourth quadrant family, while the others belong to the second. Trajectory #43 is shown in Fig. 6. This trajectory will be used as reference in the discussion of the results.

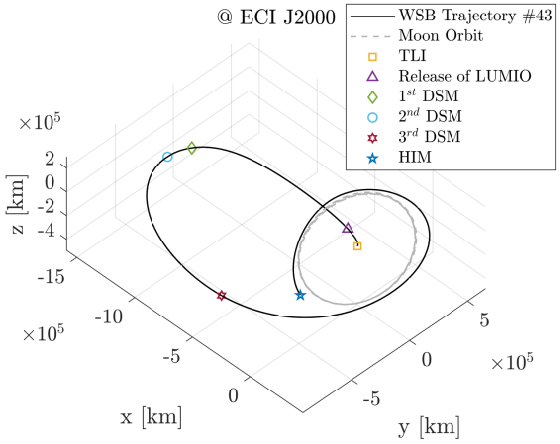

Fig. 6 LUMIO weak stability boundary transfer trajectory #43.

Finally, to ease the solution of the stochastic optimization problem in Eq. (27), analytical derivatives are implemented. The most relevant are reported in the appendix. The problem is solved with 2 different optimizers: MATLAB `fmincon`, with the *interior-point* [54] or *active-set* [55, 56] algorithms, and the sparse nonlinear optimizer (SNOPT) [57]. The choice of the algorithm is based on the convergence property of the problem. Indeed, it is heuristically found that the optimization with DG works better with the active-set algorithm, while for the OG problem SNOPT is preferred.

1. Differential Guidance Results

In Table 2, for each trajectory, the deterministic, stochastic, and total cost, ΔV_{det}, ΔV_{sto}, and ΔV_{tot}, are reported together with the final position and velocity dispersion, $\sigma_{r,n}$ and $\sigma_{v,n}$. Values are reported both for the sequential approach, used as initial guess, and the stochastic optimization approach, together with the percentage variation obtained. It is possible to see that the stochastic optimization process is able to significantly reduce the total ΔV for the transfer, while also reducing the final transfer dispersion under the imposed limits. In particular, the reduction in ΔV_{tot} is due to the decrease of ΔV_{sto}, while ΔV_{det} slightly increases. This happens for each trajectory except number #11, where the optimization produces a solution with similar ΔV_{tot} to the sequential approach result, but still reduces the final dispersion. In general, evidence shows that the process is able to obtain less fuel-expensive and, at the same time, more robust trajectories. To understand how the optimization achieves this, a maneuvers analysis is performed on trajectory #43, which is used as a representative example. The analysis is shown in Table 3, which reports, for each maneuvering event, the time of flight, the ΔV of the DSM, ΔV_{DSM}, if present, and the ΔV of the TCM, ΔV_{TCM}, computed as the 3σ value. It can be seen that the optimization reduces the cost of the TCMs, which causes the significant reduction in ΔV_{sto} seen in Table 2. It is important to note that the optimization does not directly act on ΔV_{TCM}, which is given by the differential guidance, but it rather moves the maneuvers time, as it can be seen in the time of flight column, to indirectly reduce the ΔV. In particular, for each trajectory, the first TCM is positioned as soon as possible, i.e., 6.5 days after t_0, to counteract the effects of the initial dispersion. The other TCMs can be anticipated or postponed with respect to the sequential approach, suggesting that the optimizer is able to chose the optimal TCM times to minimize ΔV_{tot}. Sometimes, the minimum maneuver distance, Δt_M, is reached. This can happen after a DSM, so that the following TCM is performed as soon as possible to counteract the increase in dispersion coming from the erroneous execution of the DSM. This happens in trajectory #02, #20, and #48. These two behaviours concerning the TCMs timing are reasonable and could have been expected even before the stochastic optimization was performed. On the other hand, this proves the good performance of the optimization. Regarding the DSMs, instead, the optimizer is able to directly act on both the maneuver magnitude, direction, and timing. With reference to trajectory #43 in Table 3, it can be seen that the DSMs magnitudes are modified, while the times are slightly adjusted. Only the time of the deterministic halo insertion maneuver is significantly modified. Indeed, the HIM is performed more than 6 days before the sequential approach result, and its ΔV moves from 0.13 to 1.19 m/s. This behavior, which is common to all considered trajectories, causes the increment on ΔV_{det} seen in Table 2. Moving the HIM time is expected to make the cost of the maneuver increase, as the optimal HIM time had been already chosen in the sequential approach. Still, the optimizer decides to always anticipate the maneuver.

To explain this behavior, a dispersion analysis is performed on each trajectory, both for the sequential approach and the stochastic optimization results. In Fig. 7, the dispersion analysis on trajectory #43 is used as a representative example of the general behavior. The trend of the dispersion is similar between the sequential approach and the stochastic

Table 2 Results of the stochastic optimization problem with differential guidance.

Trajectory ID	Approach	ΔV_{det} [m/s]	ΔV_{sto} [m/s]	ΔV_{tot} [m/s]	$\sigma_{r,n}$ [km]	$\sigma_{v,n}$ [cm/s]
#02	Sequential	47.24	20.22	67.46	12.49	6.44
	Sto. Opt. w/ DG	49.64	9.44	59.08	1.00	0.58
	Variation	+5.09%	-53.51%	-12.42%	-92.00%	-90.92%
#11	Sequential	9.66	10.05	19.72	7.18	3.02
	Sto. Opt. w/ DG	9.93	10.02	19.95	0.95	1.00
	Variation	+2.82%	-0.35%	+1.21%	-86.81%	-66.84%
#20	Sequential	42.92	16.00	58.93	2.79	1.97
	Sto. Opt. w/ DG	43.41	9.17	52.58	1.00	0.41
	Variation	+1.12%	-42.71%	-10.78%	-64.20%	-79.13%
#43	Sequential	29.96	13.07	43.03	6.64	2.91
	Sto. Opt. w/ DG	31.08	8.29	39.37	0.98	0.75
	Variation	+3.75%	-36.60%	-8.51%	-85.29%	-74.23%
#48	Sequential	41.82	18.41	60.23	6.01	2.92
	Sto. Opt. w/ DG	43.84	9.06	52.90	0.93	0.76
	Variation	+4.82%	-50.77%	-12.17%	-84.47%	-73.91%

Table 3 Maneuvers analysis on trajectory #43 optimized with differential guidance.

Maneuver ID	Time of Flight [d]		ΔV_{DSM} [m/s]		ΔV_{TCM} (3σ) [m/s]	
	Seq. App.	Sto. Opt.	Seq. App.	Sto. Opt.	Seq. App.	Sto. Opt.
#1	8.78	6.50	–	–	7.91	5.55
#2	17.56	23.39	–	–	2.86	0.83
#3	26.33	26.39	13.27	11.91	0.48	0.27
#4	35.26	35.27	15.53	16.69	2.43	2.27
#5	45.07	43.97	–	–	3.47	2.79
#6	54.88	64.56	–	–	1.42	0.65
#7	64.69	67.56	–	–	0.17	0.16
#8	74.49	74.37	1.02	1.30	0.03	0.05
#9	83.05	87.77	–	–	0.24	0.61
#10	91.61	94.59	–	–	0.15	0.47
#11	100.17	98.99	–	–	0.17	0.16
#12	108.73	102.31	0.13	1.19	–	–

optimization results, even though the placement of the TCMs, indicated with the empty dots, can be significantly different. The two behaviours differ the most in the last part of the transfer. Indeed, after the dispersion increase due to the erroneous execution of the last DSM (full dot), the stochastic optimization produces a sharp drop in the dispersion, bringing it under the covariance constraint, represented with the dashed red line: this was not achieved before with the sequential approach. In addition, by looking in particular at the position dispersion, it is possible to see that the HIM is anticipated to facilitate the matching of the dispersion constraint. In other words, the optimization trades some of the ΔV of the HIM by anticipating it, to respect the stochastic constraint, and, thus, to obtain a more robust transfer.

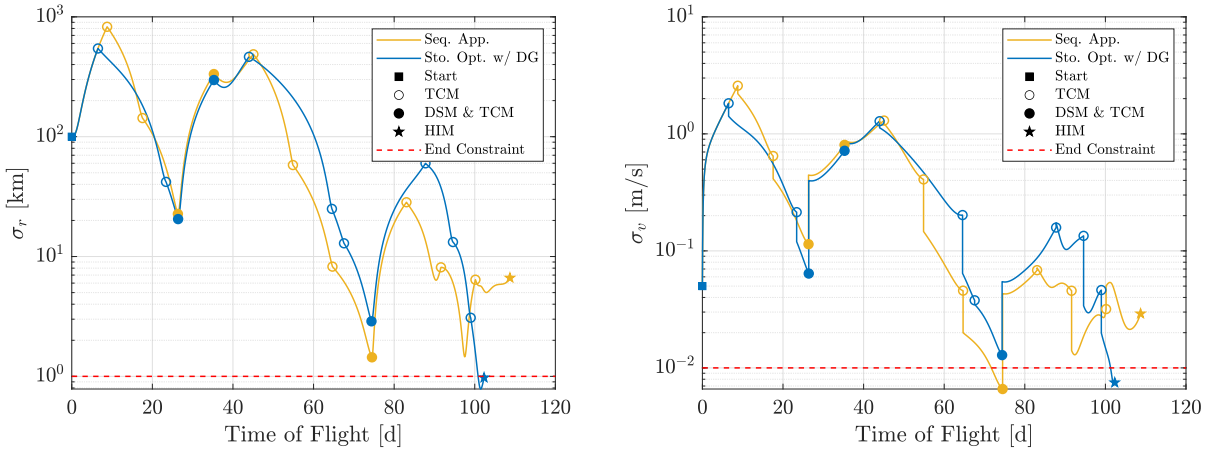

(a) 1σ Position Dispersion

(b) 1σ Velocity Dispersion

Fig. 7 Dispersion analysis on trajectory #43 optimized with differential guidance.

2. Optimal Guidance Results

The previous results are now used as initial guess for the stochastic optimization with the optimal guidance. As a remainder, this means that the elements of the guidance matrix for each TCM are completely free to move during the optimization, as they are added in the NLP vector (see Eq. (17)). In Table 4, the optimization results are reported and compared to those in Table 2, achieved with the differential guidance. The results show that optimizing also the guidance matrices further reduces the total cost of the transfers. This time the reduction comes both from ΔV_{det} and ΔV_{sto}. For the former, the optimization with OG partially reverses the increase in ΔV_{det} produced by the optimization with DG. For example, ΔV_{det} of trajectory #11 and #43 is similar to the the optimal one obtained with the sequential approach, see Table 2. Regarding the stochastic contribution, this is further reduced with respect to the DG approach, showing how OG can improve the stochastic control of the trajectory. In addition, it is interesting to notice that OG, in most cases, drives the final dispersion closer to the constraint limit, slightly increasing the dispersion with respect to the DG solution. This is probably correlated to the savings in the stochastic ΔV, as reducing the final dispersion under the limits costs fuel. This happens because, with the DG strategy, the optimizer has not full control on the

guidance matrices, which can only be tuned indirectly, by moving the TCM times. Instead, the OG strategy allows direct modification of the guidance matrices, adding degrees of freedom, which are used to relax the final dispersion and in turn save fuel. In the case of trajectory #20, this causes a final dispersion slightly above the limit. Even though from a numerical perspective this solution is unfeasible, in practice it is deemed flyable. Indeed, the final dispersion constraint is not driven by science requirements, as can be for other missions, but it is simply chosen to limit the initial dispersion on the quasi-halo orbit. Thus, all the presented OG solutions are considered appropriate for LUMIO.

Table 4 Results of the stochastic optimization problem with optimal guidance.

Trajectory ID	Approach	ΔV_{det} [m/s]	ΔV_{sto} [m/s]	ΔV_{tot} [m/s]	$\sigma_{r,n}$ [km]	$\sigma_{v,n}$ [cm/s]
#02	Sto. Opt. w/ DG	49.64	9.44	59.08	1.00	0.58
	Sto. Opt. w/ OG	48.67	8.12	56.78	0.99	1.00
	Variation	-1.96%	-14.03%	-3.89%	-1.37%	+70.82%
#11	Sto. Opt. w/ DG	9.93	10.02	19.95	0.95	1.00
	Sto. Opt. w/ OG	9.69	6.27	15.96	1.00	0.95
	Variation	-2.46%	-37.45%	-20.03%	+5.14%	-4.82%
#20	Sto. Opt. w/ DG	43.41	9.17	52.58	1.00	0.41
	Sto. Opt. w/ OG	43.37	7.48	50.85	1.08	1.05
	Variation	-0.07%	-18.48%	-3.28%	+8.09%	+154.05%
#43	Sto. Opt. w/ DG	31.08	8.29	39.37	0.98	0.75
	Sto. Opt. w/ OG	29.88	6.24	36.11	0.97	0.74
	Variation	-3.88%	-24.75%	-8.27%	-0.43%	-1.81%
#48	Sto. Opt. w/ DG	43.84	9.06	52.90	0.93	0.76
	Sto. Opt. w/ OG	42.62	7.95	50.57	1.00	1.00
	Variation	-2.78%	-12.28%	-4.41%	+7.16%	+31.20%

As done for the DG case, it is interesting to analyze the changes in each maneuver. This is done in Table 5, using trajectory #43 as reference. The maneuvering times remain similar to the ones of the DG solution, confirming that optimal times had been already obtained. Instead, the DSMs are further optimized; for instance, the third DSM (maneuver #8 in Table 5) is driven to zero. This proves that considering uncertainties inside a stochastic optimization has a direct effect also on the nominal trajectory. Indeed, the nominal trajectory output of the sequential approach was optimal under a deterministic only perspective, while now the stochastic optimizations yield a solution that is optimal from a global point of view, as both the deterministic and stochastic ΔV are considered. To get an idea of how much the nominal trajectory can change, Fig. 8 shows the position distance between the nominal trajectory #43 for both DG and OG results, and the one obtained previously in the sequential approach. Both the DG and OG results change the nominal trajectory, but the OG solution further enhance this behavior. Moreover, the OG approach is also able to reduce

the cost of the TCMs, as it can be noticed in Table 5, which ultimately results in the reduction of the stochastic ΔV. This is achieved by changing the elements of the guidance matrices, as it is shown in Table 6, that reports, as an example, the differences in the guidance matrix for maneuver #4 in trajectory #43.

Table 5 Maneuvers analysis on trajectory #43 with optimal guidance.

Maneuver ID	Time of Flight [d]		ΔV_{DSM} [m/s]		ΔV_{TCM} (3σ) [m/s]	
	DG	OG	DG	OG	DG	OG
#1	6.50	6.50	–	–	5.55	5.11
#2	23.39	23.39	–	–	0.83	0.04
#3	26.39	26.40	11.91	11.38	0.27	0.11
#4	35.27	35.27	16.69	17.07	2.27	1.37
#5	43.97	43.83	–	–	2.79	2.14
#6	64.56	64.59	–	–	0.65	0.10
#7	67.56	67.59	–	–	0.16	0.14
#8	74.37	74.37	1.30	0.00	0.05	0.36
#9	87.77	87.78	–	–	0.61	0.11
#10	94.59	94.58	–	–	0.47	0.03
#11	98.99	98.86	–	–	0.16	0.03
#12	102.31	101.86	1.19	1.43	–	–

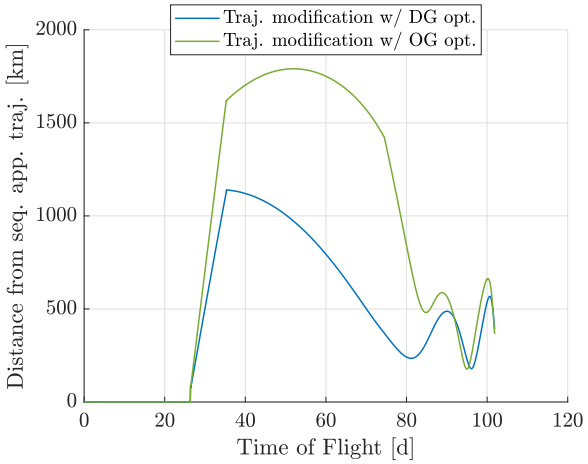

Fig. 8 Trajectory #43 modification by stochastic optimization with respect to sequential approach.

Lastly, the effects of OG on the dispersion along the transfer are analyzed. The dispersion analysis on trajectory #43 is shown in Fig. 9, and compared with the DG results. The OG solution manages to achieve a more gradual decrease in the dispersion. Indeed, the differential guidance, per its own construction, aims at minimizing the near-future deviation from the nominal trajectory. However, after a DSM is performed, the execution errors cause the dispersion to suddenly increase again, counteracting the effect of the previous TCMs. In other words, the ΔV of the first TCMs is wasted, as the dispersion returns to values similar to the initial ones after the DSMs are executed (see the behavior of the blue line

Table 6 Comparison between guidance matrices for maneuver #4 in trajectory #43.

$$\text{DG Matrix} = \begin{bmatrix} -0.4375 & 0.8339 & -0.0016 & -1.0000 & 0 & 0 \\ -0.8484 & -0.4232 & 0.0002 & 0 & -1.0000 & 0 \\ -0.0015 & 0.0008 & -0.3911 & 0 & 0 & -1.0000 \end{bmatrix}$$

$$\text{OG Matrix} = \begin{bmatrix} -0.2431 & 0.8033 & -0.0057 & -0.9786 & -0.1361 & 0.0095 \\ -0.9534 & -0.2720 & 0.0035 & 0.0993 & -0.9032 & -0.0062 \\ 0.0094 & -0.0212 & -0.0849 & 0.0032 & -0.0127 & -0.8754 \end{bmatrix}$$

around day 40). On the contrary, the optimal guidance avoids this problem by limiting the dispersion reduction before the DSMs. Thus, in the first part of the transfer, the dispersion is kept under control by only counteracting its increase due to DSMs executions, while the main dispersion reduction happens only in the last part of the transfer, to satisfy the final constraints. This mechanism allows minimizing the stochastic ΔV.

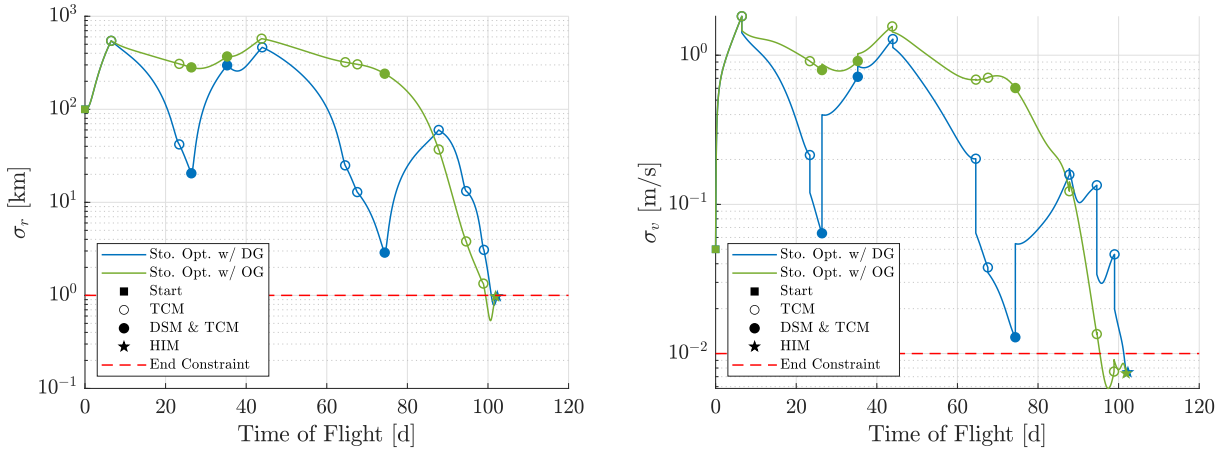

(a) 1σ Position Dispersion

(b) 1σ Velocity Dispersion

Fig. 9 Dispersion analysis on trajectory #20 with optimal guidance.

Finally, the results in terms of ΔV of the 3 approaches (i.e., the sequential approach, the stochastic optimizations with DG and OG) are visually compared in Fig. 10. With respect to the sequential approach, the optimization with the differential guidance saves on average 8.53% of the total ΔV, while the optimal guidance further increase the savings up to an average of 16.14%. These results highlight the beneficial effects that trajectory optimization under uncertainty can have for mission analysis.

B. Monte Carlo Validation

In this section, the results of the stochastic optimizations, both in terms of ΔV and dispersion analysis, are validated with Monte Carlo simulations. The Monte Carlo analyses share the same quantitative data reported in Table 1, but

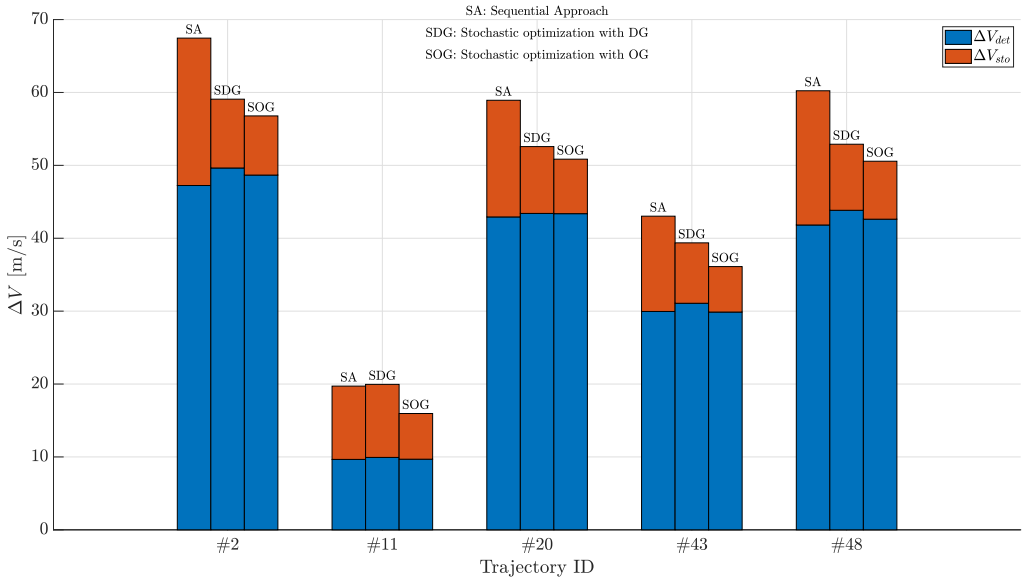

Fig. 10 ΔV comparison between the sequential approach and the stochastic optimization with DG and OG.

implement each uncertainty by random extraction from its relative Gaussian distribution, which is done for each sample. While this allows an analogous implementation to the unscented transformation methodology of the initial conditions and DSM execution errors, it also enables the application of an independent navigation error for each TCM, increasing the realism of the simulation. In addition, process noise is considered as a further source of uncertainty. Both solar radiation pressure and the residual accelerations are modeled as Gauss–Markov processes (see Section II.A); their characteristics, in terms of standard deviation, σ, and correlation time, τ, are listed in Table 7. Finally, instead of using the 3σ value in the computation of the stochastic ΔV (Eq. 20), in the Monte Carlo simulations the 99.73 percentile is implemented to further increase realism.

Table 7 Gauss–Markov Processes Characteristics.

Gauss–Markov Process	σ	τ
Solar Radiation Pressure	5% in magnitude	1 d
Residual Acceleration	10^{-12} km/s^2	1 d

The simulations are run for each results of the stochastic optimization, both for the differential and optimal guidance, with a population size of 10,000 samples. However, only results regarding OG are shown here for brevity, as they are more significant due to the additional nonlinearity related to the optimal guidance matrices, which could cause, in theory, a less accurate prediction by the unscented transformation. Results, reported in Table 8, show that the unscented transformation is able to make a good prediction of the total ΔV and final position and velocity dispersion. Some differences were expected, due to the high nonlinearity of the problem, and the additional accuracy of the Monte Carlo

simulations. Nonetheless, the ΔV_{tot} predicted by the unscented transformation has, on average, a relative error of 0.94% with respect to the Monte Carlo results, which are assumed as the truth. This is regarded as an excellent result, given that the main aim is to minimize the ΔV, which, as a consequence, shall be predicted by the uncertainty propagation method with high accuracy, which is the case. A small underestimation is, instead, seen on the unscented transformation predictions for the final dispersion. The relative error with the Monte Carlo results is, on average, 32.21% and 17.31%, for the final dispersion in position and velocity, respectively. The difference may seem relevant, but this is because a relative error is considered on quantities that are constrained to be small. Indeed, by looking at the absolute error on the dispersion analysis during the whole transfer, which is shown in Fig. 11 with trajectory #43 as a representative example, one can conclude that the unscented transformation prediction is quite accurate. Indeed, the maximum error is below 3 km for dispersion in position, and 1 cm/s in velocity, which are small values for mission analysis purposes. Moreover, the error is maximum in the initial part of the transfer, before the first TCM is applied, and, then, it decreases towards 0.

Table 8 Results of the Monte Carlo simulations on the optimal guidance solutions. Monte Carlo analyses additionally implement process noise and multiple navigation errors.

		ΔV_{tot} [m/s]	$\sigma_{r,n}$ [km]	$\sigma_{r,n}$ [cm/s]
Trajectory #02	UT	56.78	0.99	1.00
	MC	57.70	1.56	1.12
Trajectory #11	UT	15.96	1.00	0.95
	MC	16.18	1.14	0.99
Trajectory #20	UT	50.85	1.08	1.05
	MC	51.12	1.47	1.32
Trajectory #43	UT	36.11	0.97	0.74
	MC	36.54	1.22	0.90
Trajectory #48	UT	50.57	1.00	1.00
	MC	50.55	2.79	1.49

To further validate the unscented transformation predictions, the final position distribution, relevant for the halo insertion maneuver, is analyzed. In Fig. 12, the distribution coming from the Monte Carlo simulation is shown alongside the 3σ ellipsoid predicted by the unscented transformation. The color scale represents the probability density function, with darker colors indicating regions where the final position is more likely to occur. The shape and colors of the distribution show that it remains similar to the normal one, with the majority of the points inside the 3σ ellipsoid: for this reason, the unscented transformation prediction is deemed a good estimate of the real final distribution.

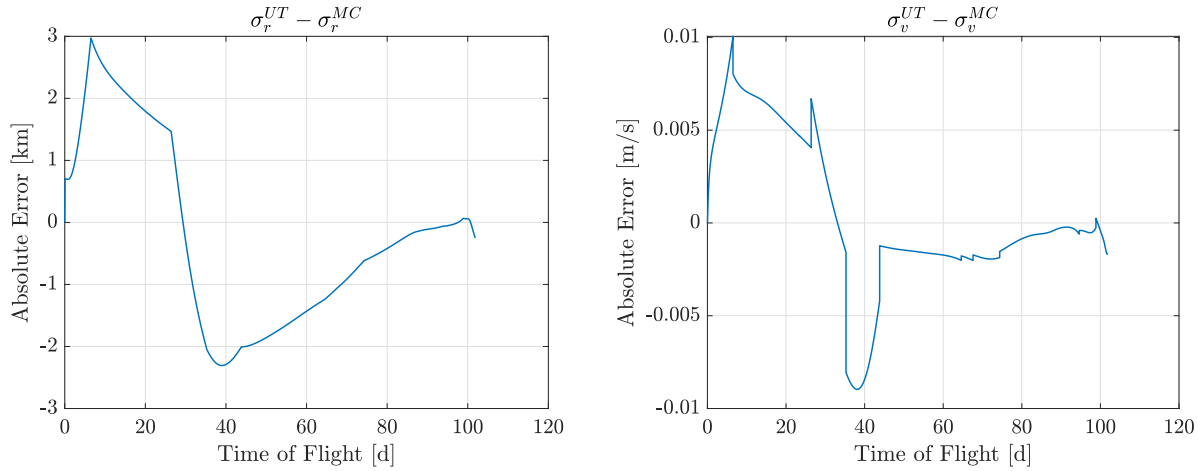

(a) Position Dispersion Error

(b) Velocity Dispersion Error

Fig. 11 Absolute error between UT and MC on the dispersion analysis on trajectory #43.

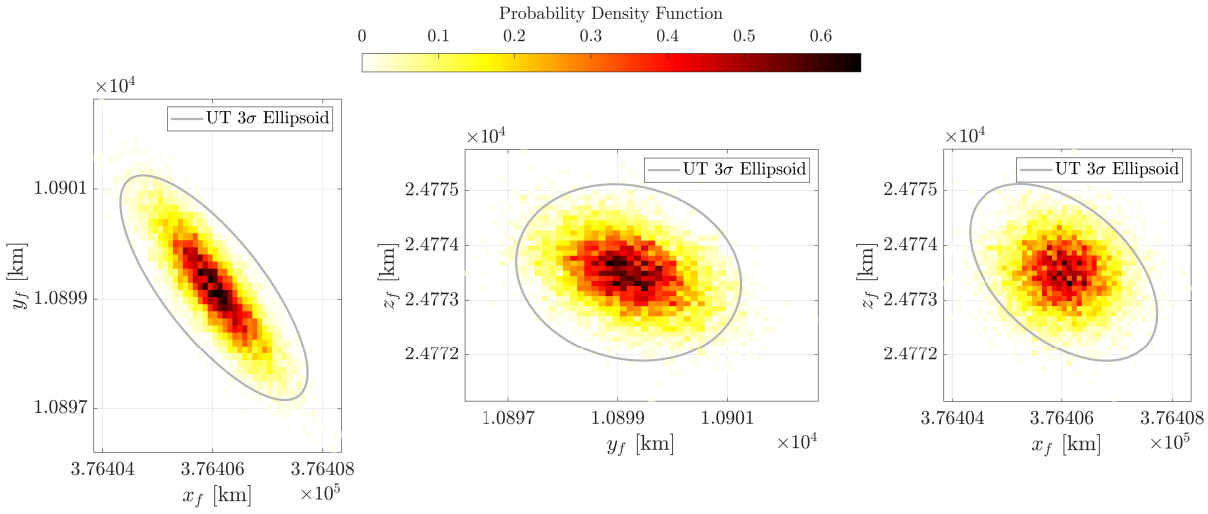

Fig. 12 Final position distribution of trajectory #43, plotted in the rotating frame for each plane section.

IV. Conclusion

This work introduces a method for stochastic trajectory optimization that accounts for uncertainties in initial conditions, maneuvers, and navigation errors. A novel implementation of the unscented transformation leverages a continuous propagation map to avoid resampling, which improves accuracy. The stochastic problem is reformulated as a deterministic nonlinear programming problem, solvable with gradient-based optimization techniques. Tested on several weak stability boundary transfers of the LUMIO mission, the method shows average fuel savings of 16.14% compared to traditional approaches, while also improving robustness. This is achieved thanks to an optimal placement in time of correction maneuvers, and a smarter dispersion control that avoids wasting fuel in the initial and final part of the transfer. Validation through Monte Carlo analyses confirms the method's accuracy.

The research presented in this paper highlights the beneficial effects of stochastic trajectory optimization for mission analysis applications. An improved solution, with respect to the one obtainable with conventional deterministic optimization, can be attained by considering uncertainty inside the optimization phase. The proposed methodology is particularly suitable for transfer trajectories in nonlinear or perturbed dynamical environments. The minimum number of samples required by the unscented transformation enables the solution of the stochastic optimization problem without the need of huge computational power. At the same time, its novel implementation through a continuous propagation map assures good accuracy in the predictions of the fuel cost and the stochastic moments of the state, despite the high nonlinearity of the problem and the long propagation times. Finally, the benefits of this approach are particularly useful for spacecraft with limited control authority and fuel budget, such as CubeSats, but are also applicable to other mission scenarios.

Appendix: Relevant Analytical Derivatives

To solve the optimization problem reported in Eq. (27), analytical derivatives of the objective function and constraints are needed. To compute them, the chain-rule is extensively used and the objective function and constraints are expressed as function of the NLP variables. In this appendix, only the relevant analytical derivatives are shown.

A. Dynamical Derivatives

With reference to Eq. (28), the equations of motion are rewritten as $\boldsymbol{x}' = \boldsymbol{f}(\boldsymbol{x}, t)$, where $\boldsymbol{x} = [\boldsymbol{r}, \boldsymbol{r}']$ and the symbol ($'$) indicates a derivative with respect to the non-dimensional time. The Jacobian, defined as $\boldsymbol{A}(t) = \dfrac{\partial \boldsymbol{f}(\boldsymbol{x}, t)}{\partial \boldsymbol{x}}$, is computed as [49]

$$\boldsymbol{A}(t) = \begin{bmatrix} \boldsymbol{0}_3 & \boldsymbol{I}_3 \\ -\dfrac{1}{n^2}\left(\dfrac{\ddot{k}}{k} I + 2\dfrac{\dot{k}}{k} C^\top \dot{C} + C^\top \ddot{C}\right) + G\dfrac{m_1 + m_2}{n^2 k^3}\dfrac{\partial(\boldsymbol{\nabla}\Omega)}{\partial \boldsymbol{r}} + \dfrac{\partial \boldsymbol{a}_{SRP}}{\partial \boldsymbol{r}} & -\dfrac{2}{n}\left(\dfrac{\dot{k}}{k} I + C^\top \dot{C}\right) \end{bmatrix} \tag{A1}$$

where the symbol ($\dot{}$) indicates a derivative with respect to the dimensional time, and the gradient of the pseudo-potential, Ω, is $\boldsymbol{\nabla}\Omega = G\frac{m_1+m_2}{n^2k^3}\left[(1-\mu)\,\frac{\boldsymbol{r}-\boldsymbol{r}_1}{\|\boldsymbol{r}-\boldsymbol{r}_1\|^3} + \mu\frac{\boldsymbol{r}-\boldsymbol{r}_2}{\|\boldsymbol{r}-\boldsymbol{r}_2\|^3} + \sum_j \hat{\mu}_j \frac{\boldsymbol{r}-\boldsymbol{r}_j}{\|\boldsymbol{r}-\boldsymbol{r}_j\|^3}\right]$.

Considering a state $\boldsymbol{x}_1$ at time t_1, the flow $\boldsymbol{\varphi}$ of the equations of motion at time t_2 is defined as $\boldsymbol{x}\,(t_2) = \boldsymbol{\varphi}\,(\boldsymbol{x}_1, t_1, t_2)$. The derivatives of the flow are computed as [58]

$$\frac{\partial \boldsymbol{\varphi}\,(\boldsymbol{x}_1, t_1, t_2)}{\partial \boldsymbol{x}_1} = \boldsymbol{\Phi}\,(\boldsymbol{x}_1, t_1, t_2) \tag{A2}$$

$$\frac{\partial \boldsymbol{\varphi}\,(\boldsymbol{x}_1, t_1, t_2)}{\partial t_1} = -\boldsymbol{\Phi}\,(\boldsymbol{x}_1, t_1, t_2)\,\boldsymbol{f}\,(\boldsymbol{x}_1, t_1) \tag{A3}$$

$$\frac{\partial \boldsymbol{\varphi}\,(\boldsymbol{x}_1, t_1, t_2)}{\partial t_2} = \boldsymbol{f}\,(\boldsymbol{\varphi}\,(\boldsymbol{x}_1, t_1, t_2), t_2) \tag{A4}$$

where the state transition matrix, $\boldsymbol{\Phi}$, is integrated alongside the equations of motion with $\boldsymbol{\Phi}'\,(\boldsymbol{x}_1, t_1, t) = \boldsymbol{A}\,(t)\,\boldsymbol{\Phi}\,(\boldsymbol{x}_1, t_1, t)$. The derivatives of the state transition matrix are

$$\frac{\partial \boldsymbol{\Phi}\,(\boldsymbol{x}_1, t_1, t_2)}{\partial \boldsymbol{x}_1} = \boldsymbol{\Theta}\,(\boldsymbol{x}_1, t_1, t_2) \tag{A5}$$

$$\begin{aligned}\frac{\partial \boldsymbol{\Phi}\,(\boldsymbol{x}_1, t_1, t_2)}{\partial t_1} &= \frac{\partial}{\partial t_1}\left(\frac{\partial \boldsymbol{\varphi}\,(\boldsymbol{x}_1, t_1, t_2)}{\partial \boldsymbol{x}_1}\right) = \frac{\partial}{\partial \boldsymbol{x}_1}\left(\frac{\partial \boldsymbol{\varphi}\,(\boldsymbol{x}_1, t_1, t_2)}{\partial t_1}\right) = \frac{\partial\left(-\boldsymbol{\Phi}\,(\boldsymbol{x}_1, t_1, t_2)\,\boldsymbol{f}\,(\boldsymbol{x}_1, t_1)\right)}{\partial \boldsymbol{x}_1} = \\ &= -\boldsymbol{\Theta}\,(\boldsymbol{x}_1, t_1, t_2)\,\boldsymbol{f}\,(\boldsymbol{x}_1, t_1) - \boldsymbol{\Phi}\,(\boldsymbol{x}_1, t_1, t_2)\,\boldsymbol{A}\,(t_1)\end{aligned} \tag{A6}$$

$$\begin{aligned}\frac{\partial \boldsymbol{\Phi}\,(\boldsymbol{x}_1, t_1, t_2)}{\partial t_2} &= \frac{\partial}{\partial t_2}\left(\frac{\partial \boldsymbol{\varphi}\,(\boldsymbol{x}_1, t_1, t_2)}{\partial \boldsymbol{x}_1}\right) = \frac{\partial}{\partial \boldsymbol{x}_1}\left(\frac{\partial \boldsymbol{\varphi}\,(\boldsymbol{x}_1, t_1, t_2)}{\partial t_2}\right) = \frac{\partial \boldsymbol{f}\,(\boldsymbol{\varphi}\,(\boldsymbol{x}_1, t_1, t_2), t_2)}{\partial \boldsymbol{x}_1} = \\ &= \frac{\partial \boldsymbol{f}\,(\boldsymbol{\varphi}\,(\boldsymbol{x}_1, t_1, t_2), t_2)}{\partial \boldsymbol{\varphi}\,(\boldsymbol{x}_1, t_1, t_2)}\frac{\partial \boldsymbol{\varphi}\,(\boldsymbol{x}_1, t_1, t_2)}{\partial \boldsymbol{x}_1} = \\ &= \boldsymbol{A}\,(t_2)\,\boldsymbol{\Phi}\,(\boldsymbol{x}_1, t_1, t_2)\end{aligned} \tag{A7}$$

where $\boldsymbol{\Theta}$ is a third order tensor, whose components are numerically computed with the second order central difference

$$\Theta_{\alpha\beta\gamma} = \frac{\partial \Phi_{\alpha\beta}}{\partial x_\gamma} \approx \frac{\Phi_{\alpha\beta}\left(x_\gamma + \varepsilon\right) - \Phi_{\alpha\beta}\left(x_\gamma - \varepsilon\right)}{2\varepsilon} \tag{A8}$$

B. Differential Guidance Derivative

With reference to Eq. (16), a generic differential guidance matrix is rewritten as $\boldsymbol{G} = -\left[\boldsymbol{Q}^{-1}\boldsymbol{R}, \boldsymbol{I}_3\right]$. Its derivative with respect to a generic variable, $\partial\boldsymbol{G}$, is computed as

$$\partial\boldsymbol{G} = -\left[\partial\boldsymbol{Q}^{-1}\boldsymbol{R} + \boldsymbol{Q}^{-1}\partial\boldsymbol{R}, \boldsymbol{0}_3\right] = -\left[-\boldsymbol{Q}^{-1}\partial\boldsymbol{Q}\boldsymbol{Q}^{-1}\boldsymbol{R} + \boldsymbol{Q}^{-1}\partial\boldsymbol{R}, \boldsymbol{0}_3\right] \tag{A9}$$

where:

$$\partial \boldsymbol{Q} = \partial \boldsymbol{\Phi}_{rv}^{\top} \boldsymbol{\Phi}_{rv} + \boldsymbol{\Phi}_{rv}^{\top} \partial \boldsymbol{\Phi}_{rv} + q \left(\partial \boldsymbol{\Phi}_{vv}^{\top} \boldsymbol{\Phi}_{vv} + \boldsymbol{\Phi}_{vv}^{\top} \partial \boldsymbol{\Phi}_{vv} \right) \tag{A10}$$

$$\partial \boldsymbol{R} = \partial \boldsymbol{\Phi}_{rv}^{\top} \boldsymbol{\Phi}_{rr} + \boldsymbol{\Phi}_{rv}^{\top} \partial \boldsymbol{\Phi}_{rr} + q \left(\partial \boldsymbol{\Phi}_{vv}^{\top} \boldsymbol{\Phi}_{vr} + \boldsymbol{\Phi}_{vv}^{\top} \partial \boldsymbol{\Phi}_{vr} \right) \tag{A11}$$

C. Square Root Matrix Derivative

To compute the initial sigma points, as indicated in Eq. (6), the square root of the matrix $(N + \lambda)\, \boldsymbol{\mathcal{P}}_0$ is needed. Since $\boldsymbol{\mathcal{P}}_0$ depends on the nominal open-loop maneuvers, which are directly part of the NLP vector, the derivative of the square root matrix is also needed. Considering a generic square matrix $\boldsymbol{M}$, its square root matrix, $\sqrt{\boldsymbol{M}}$, is such that $\boldsymbol{M} = \sqrt{\boldsymbol{M}} \sqrt{\boldsymbol{M}}$. The generic derivative of $\boldsymbol{M}$, $\partial \boldsymbol{M}$, is computed as

$$\partial \boldsymbol{M} = \partial \sqrt{\boldsymbol{M}} \sqrt{\boldsymbol{M}} + \sqrt{\boldsymbol{M}} \partial \sqrt{\boldsymbol{M}} \tag{A12}$$

Following [2], it is possible to consider Eq. (A12) as a special case of the Sylvester equation:

$$\boldsymbol{A}\boldsymbol{X} + \boldsymbol{X}\boldsymbol{B} = \boldsymbol{C} \tag{A13}$$

with $\boldsymbol{A} = \boldsymbol{B} = \partial \sqrt{\boldsymbol{M}}$, $\boldsymbol{C} = \partial \boldsymbol{M}$, and $\boldsymbol{X} = \sqrt{\boldsymbol{M}}$. Equation (A13) can be solved as [59]

$$\left(\boldsymbol{I} \otimes \boldsymbol{A} + \boldsymbol{B}^{\top} \otimes \boldsymbol{I} \right) \mathrm{vec}\left(\boldsymbol{X} \right) = \mathrm{vec}\left(\boldsymbol{C} \right) \tag{A14}$$

where $\boldsymbol{I}$ is the identity matrix, and $\mathrm{vec}\left(\cdot\right)$ is the vectorization function. Applying to Eq. (A14) the special case of the square root matrix, and using the definition of the Kronecker sum, $\oplus$, yields

$$\mathrm{vec}\left(\partial \sqrt{\boldsymbol{M}} \right) = \left(\sqrt{\boldsymbol{M}}^{\top} \oplus \sqrt{\boldsymbol{M}} \right)^{-1} \mathrm{vec}\left(\partial \boldsymbol{M} \right) \tag{A15}$$

Funding Sources

Part of the work described in this paper has been funded by the European Space Agency under the General Support Technology Programme (GSTP), ESA contract No. 4000139301/22/NL/AS, and has received support from the national delegations of Italy (through ASI's ALCOR program) and Norway.

References

[1] Fehse, W., *Automated Rendezvous and Docking of Spacecraft*, Cambridge Aerospace Series, Cambridge University Press, 2003, pp. 79–80. https://doi.org/10.1017/CBO9780511543388.

[2] Giordano, C., and Topputo, F., "Analysis, Design, and Optimization of Robust Trajectories in Cislunar Environment for Limited-Capability Spacecraft," *The Journal of the Astronautical Sciences*, Vol. 70, No. 6, 2023, pp. 1–56. https://doi.org/10.1007/s40295-023-00413-8.

[3] Walker, R., Binns, D., Bramanti, C., Casasco, M., Concari, P., Izzo, D., Feili, D., Fernandez, P., Fernandez, J. G., Hager, P., Koschny, D., Pesquita, V., Wallace, N., Carnelli, I., Khan, M., Scoubeau, M., and Taubert, D., "Deep-space CubeSats: thinking inside the box," *Astronomy & Geophysics*, Vol. 59, No. 5, 2018, pp. 5.24–5.30. https://doi.org/10.1093/astrogeo/aty232.

[4] Russell, R. P., "Survey of Spacecraft Trajectory Design in Strongly Perturbed Environments," *Journal of Guidance, Control, and Dynamics*, Vol. 35, No. 3, 2012, pp. 705–720. https://doi.org/10.2514/1.56813.

[5] Belbruno, E. A., and Miller, J. K., "Sun-Perturbed Earth-to-Moon Transfers with Ballistic Capture," *Journal of Guidance, Control, and Dynamics*, Vol. 16, No. 4, 1993, pp. 770–775. https://doi.org/10.2514/3.21079.

[6] Gómez, G., Llibre, J., Martínez, R., and Simó, C., *Dynamics and Mission Design Near Libration Points-Vol I: Fundamentals: The Case of Collinear Libration Points*, World Scientific, 2001, Vol. 2, Chap. 1. https://doi.org/10.1142/4402.

[7] Scheeres, D. J., *Orbital Motion in Strongly Perturbed Environments*, Springer Berlin Heidelberg, Berlin, Heidelberg, 2012, Chap. 2, pp. 23–59. https://doi.org/10.1007/978-3-642-03256-1.

[8] Fleming, W. H., and Rishel, R. W., *Deterministic and Stochastic Optimal Control*, Springer Science & Business Media, 2012, Vol. 1, Chap. 6. https://doi.org/10.1007/978-1-4612-6380-7.

[9] Bellman, R., *Dynamic Programming*, Princeton University Press, 1957, Chap. 3.

[10] Yong, J., and Zhou, X. Y., *Stochastic Controls: Hamiltonian Systems and HJB Equations*, Springer Science & Business Media, 2012, Vol. 43, pp. 182–184. https://doi.org/10.1007/978-1-4612-1466-3.

[11] Gustafson, E. D., "Stochastic Optimal Control of Spacecraft," Ph.D. thesis, University of Michigan, 2010. https://deepblue.lib.umich.edu/handle/2027.42/77707.

[12] Kappen, H. J., "Linear Theory for Control of Nonlinear Stochastic Systems," *Phys. Rev. Lett.*, Vol. 95, No. 20, 2005, pp. 1–4. https://doi.org/10.1103/PhysRevLett.95.200201.

[13] Mayne, D. Q., "Differential Dynamic Programming – A Unified Approach to the Optimization of Dynamic Systems," Academic Press, 1973, pp. 179–254. https://doi.org/10.1016/B978-0-12-012710-8.50010-8.

[14] Theodorou, E., Tassa, Y., and Todorov, E., "Stochastic Differential Dynamic Programming," *Proceedings of the 2010 American Control Conference*, Baltimore, MD, 2010, pp. 1125–1132. https://doi.org/10.1109/ACC.2010.5530971.

[15] Luo, Y. Z., and Yang, Z., "A review of uncertainty propagation in orbital mechanics," *Progress in Aerospace Sciences*, Vol. 89, 2017, pp. 23–39. https://doi.org/10.1016/j.paerosci.2016.12.002.

[16] Maybeck, P. S., *Stochastic models, estimation, and control*, Academic Press, 1982, Chaps. 4–5.

[17] Ono, M., Williams, B. C., and Blackmore, L., "Probabilistic Planning for Continuous Dynamic Systems Under Bounded Risk," *Journal of Artificial Intelligence Research*, Vol. 46, 2013, pp. 511–577. https://doi.org/10.1613/jair.3893.

[18] Okamoto, K., Goldshtein, M., and Tsiotras, P., "Optimal Covariance Control for Stochastic Systems Under Chance Constraints," *IEEE Control Systems Letters*, Vol. 2, No. 2, 2018, pp. 266–271. https://doi.org/10.1109/LCSYS.2018.2826038.

[19] Kelly, S., and Geller, D., "Robust Cislunar Trajectory Optimization in the Presence of Stochastic Errors," *The Journal of the Astronautical Sciences*, Vol. 71, No. 4, 2024, pp. 1–46. https://doi.org/10.1007/s40295-024-00450-x.

[20] Ross, I. M., Proulx, R. J., and Karpenko, M., "Unscented Optimal Control for Space Flight," *24th International Symposium on Space Flight Dynamics (ISSFD)*, Laurel, MD, 2014, pp. 1–12.

[21] Julier, S., Uhlmann, J., and Durrant-Whyte, H., "A New Approach for Filtering Nonlinear Systems," *Proceedings of 1995 American Control Conference - ACC'95*, Vol. 3, Seattle, WA, 1995, pp. 1628–1632. https://doi.org/10.1109/ACC.1995.529783.

[22] Marmo, N., and Zavoli, A., "Chance-constraint optimization of interplanetary trajectories with a hybrid multiple-shooting approach," *2022 AAS/AIAA Astrodynamics Specialist Conference*, Charlotte, NC, 2022, pp. 1–18.

[23] Marmo, N., Zavoli, A., Ozaki, N., and Kawakatsu, Y., "A hybrid multiple-shooting approach for covariance control of interplanetary missions with navigation errors," *33rd AAS/AIAA Space Flight Mechanics Meeting*, Austin, TX, 2023, pp. 1–20.

[24] Ozaki, N., Campagnola, S., and Funase, R., "Tube Stochastic Optimal Control for Nonlinear Constrained Trajectory Optimization Problems," *Journal of Guidance, Control, and Dynamics*, Vol. 43, No. 4, 2020, pp. 645–655. https://doi.org/10.2514/1.G004363.

[25] Oguri, K., and McMahon, J. W., "Robust Spacecraft Guidance Around Small Bodies Under Uncertainty: Stochastic Optimal Control Approach," *Journal of Guidance, Control, and Dynamics*, Vol. 44, No. 7, 2021, pp. 1295–1313. https://doi.org/10.2514/1.G005426.

[26] Ridderhof, J., Pilipovsky, J., and Tsiotras, P., "Chance-constrained covariance control for low-thrust minimum-fuel trajectory optimization," *2020 AAS/AIAA Astrodynamics Specialist Conference*, South Lake Tahoe, CA, 2020, pp. 1–20.

[27] Jones, B. A., Doostan, A., and Born, G. H., "Nonlinear Propagation of Orbit Uncertainty Using Non-Intrusive Polynomial Chaos," *Journal of Guidance, Control, and Dynamics*, Vol. 36, No. 2, 2013, pp. 430–444. https://doi.org/10.2514/1.57599.

[28] Xiong, F., Xiong, Y., and Xue, B., "Trajectory Optimization under Uncertainty based on Polynomial Chaos Expansion," *AIAA Guidance, Navigation, and Control Conference*, Kissimmee, FL, 2015, pp. 1–15. https://doi.org/10.2514/6.2015-1761.

[29] Adurthi, N., Singla, P., and Singh, T., "Conjugate Unscented Transformation: Applications to Estimation and Control," *Journal of Dynamic Systems, Measurement, and Control*, Vol. 140, No. 3, 2017, pp. 1–22. https://doi.org/10.1115/1.4037783.

[30] Greco, C., Campagnola, S., and Vasile, M., "Robust Space Trajectory Design Using Belief Optimal Control," *Journal of Guidance, Control, and Dynamics*, Vol. 45, No. 6, 2022, pp. 1060–1077. https://doi.org/10.2514/1.G005704.

[31] Valli, M., Armellin, R., Di Lizia, P., and Lavagna, M. R., "Nonlinear Mapping of Uncertainties in Celestial Mechanics," *Journal of Guidance, Control, and Dynamics*, Vol. 36, No. 1, 2013, pp. 48–63. https://doi.org/10.2514/1.58068.

[32] Di Lizia, P., Armellin, R., Bernelli-Zazzera, F., and Berz, M., "High order optimal control of space trajectories with uncertain boundary conditions," *Acta Astronautica*, Vol. 93, 2014, pp. 217–229. https://doi.org/10.1016/j.actaastro.2013.07.007.

[33] Fu, X., Baresi, N., and Armellin, R., "Stochastic optimization for stationkeeping of periodic orbits using a high-order Target Point Approach," *Advances in Space Research*, Vol. 70, No. 1, 2022, pp. 96–111. https://doi.org/10.1016/j.asr.2022.04.039.

[34] Terejanu, G., Singla, P., Singh, T., and Scott, P. D., "Uncertainty Propagation for Nonlinear Dynamic Systems Using Gaussian Mixture Models," *Journal of Guidance, Control, and Dynamics*, Vol. 31, No. 6, 2008, pp. 1623–1633. https://doi.org/10.2514/1.36247.

[35] Boone, S., and McMahon, J., "Spacecraft maneuver design with non-gaussian chance constraints using gaussian mixtures," *2022 AAS/AIAA Astrodynamics Specialist Conference*, Charlotte, NC, 2022, pp. 1–19.

[36] Park, R. S., and Scheeres, D. J., "Nonlinear Mapping of Gaussian Statistics: Theory and Applications to Spacecraft Trajectory Design," *Journal of Guidance, Control, and Dynamics*, Vol. 29, No. 6, 2006, pp. 1367–1375. https://doi.org/10.2514/1.20177.

[37] Betts, J. T., "Survey of Numerical Methods for Trajectory Optimization," *Journal of guidance, control, and dynamics*, Vol. 21, No. 2, 1998, pp. 193–207. https://doi.org/10.2514/2.4231.

[38] Topputo, F., Merisio, G., Franzese, V., Giordano, C., Massari, M., Pilato, G., Labate, D., Cervone, A., Speretta, S., Menicucci, A., Turan, E., Bertels, E., Vennekens, J., Walker, R., and Koschny, D., "Meteoroids detection with the LUMIO lunar CubeSat," *Icarus*, Vol. 389, 2023, pp. 1–19. https://doi.org/10.1016/j.icarus.2022.115213.

[39] Giordano, C., Martinelli, A., Buonagura, C., Merisio, G., Franzese, V., and Topputo, F., "Trajectory design and analysis of the LUMIO CubeSat," *AIAA Scitech 2024 Forum*, Orlando, FL, 2024, pp. 1–12. https://doi.org/10.2514/6.2024-1271.

[40] Schutz, B., Tapley, B., and Born, G. H., *Statistical Orbit Determination*, Elsevier, 2004, Chap. 4, pp. 230–233. https://doi.org/10.1016/B978-0-12-683630-1.X5019-X.

[41] Lemons, D. S., and Gythiel, A., "Paul Langevin's 1908 paper "On the Theory of Brownian Motion" ["Sur la théorie du mouvement brownien," C. R. Acad. Sci. (Paris) 146, 530-533 (1908)]," *American Journal of Physics*, Vol. 65, No. 11, 1997, pp. 1079–1081. https://doi.org/10.1119/1.18725.

[42] Giordano, C., "Characterization of Gauss–Markov stochastic sequences for mission analysis," *Astrodynamics*, Vol. 8, No. 1, 2024, pp. 135–148. https://doi.org/10.1007/s42064-023-0183-3.

[43] Bertsekas, D., and Shreve, S. E., *Stochastic Optimal Control: The Discrete-Time Case*, Athena Scientific, 1996, Chap. 1, p. 6.

[44] Dei Tos, D. A., Rasotto, M., Renk, F., and Topputo, F., "LISA Pathfinder mission extension: A feasibility analysis," *Advances in Space Research*, Vol. 63, No. 12, 2019, pp. 3863–3883. https://doi.org/10.1016/j.asr.2019.02.035.

[45] Cipriano, A. M., Tos, D. A. D., and Topputo, F., "Orbit Design for LUMIO: The Lunar Meteoroid Impacts Observer," *Frontiers in Astronomy and Space Sciences*, Vol. 5, 2018, pp. 1–23. https://doi.org/10.3389/fspas.2018.00029.

[46] Dei Tos, D. A., and Topputo, F., "On the advantages of exploiting the hierarchical structure of astrodynamical models," *Acta Astronautica*, Vol. 136, 2017, pp. 236–247. https://doi.org/10.1016/j.actaastro.2017.02.025.

[47] Szebehely, V., *Theory of orbit: The restricted problem of three Bodies*, Academic Press, 1967, Chap. 1. https://doi.org/10.1016/B978-0-12-395732-0.X5001-6.

[48] Gómez, G., Masdemont, J. J., and Mondelo, J. M., "Solar system models with a selected set of frequencies," *Astronomy & Astrophysics*, Vol. 390, No. 2, 2002, pp. 733–749. https://doi.org/10.1051/0004-6361:20020625.

[49] Dei Tos, D. A., "Automated Trajectory Refinement of Three-Body Orbits in the Real Solar System Model," Master's thesis, Politecnico di Milano, 2014. https://www.politesi.polimi.it/handle/10589/93675.

[50] Folkner, W. M., "Planetary ephemeris DE432," Interoffice Memorandum 392R-14-003, Jet Propulsion Laboratory, April 2014.

[51] Acton, C. H., "Ancillary data services of NASA's Navigation and Ancillary Information Facility," *Planetary and Space Science*, Vol. 44, No. 1, 1996, pp. 65–70. https://doi.org/10.1016/0032-0633(95)00107-7.

[52] Acton, C., Bachman, N., Semenov, B., and Wright, E., "A look towards the future in the handling of space science mission geometry," *Planetary and Space Science*, Vol. 150, 2018, pp. 9–12. https://doi.org/10.1016/j.pss.2017.02.013.

[53] Circi, C., and Teofilatto, P., "On the Dynamics of Weak Stability Boundary Lunar Transfers," *Celestial Mechanics and Dynamical Astronomy*, Vol. 79, 2001, pp. 41–72. https://doi.org/10.1023/A:1011153610564.

[54] Byrd, R. H., Hribar, M. E., and Nocedal, J., "An Interior Point Algorithm for Large-Scale Nonlinear Programming," *SIAM Journal on Optimization*, Vol. 9, No. 4, 1999, pp. 877–900. https://doi.org/10.1137/S1052623497325107.

[55] Biggs, M., "Constrained Minimization Using Recursive Quadratic Programming," *Towards global optimization*, North-Holland, 1975, pp. 341–349.

[56] Fletcher, R., *Practical methods of optimization*, John Wiley & Sons, 1987, Chap. 10. https://doi.org/10.1002/9781118723203.

[57] Gill, P. E., Murray, W., and Saunders, M. A., "SNOPT: An SQP Algorithm for Large-Scale Constrained Optimization," *SIAM Journal on Optimization*, Vol. 12, No. 4, 2002, pp. 979–1006. https://doi.org/10.1137/S1052623499350013.

[58] Dei Tos, D. A., and Topputo, F., "High-Fidelity Trajectory Optimization with Application to Saddle-Point Transfers," *Journal of Guidance, Control, and Dynamics*, Vol. 42, No. 6, 2019, pp. 1343–1352. https://doi.org/10.2514/1.G003838.

[59] Bartels, R. H., and Stewart, G. W., "Solution of the matrix equation AX + XB = C [F4]," *Commun. ACM*, Vol. 15, No. 9, 1972, pp. 820–826. https://doi.org/10.1145/361573.361582.